

## The Zhaxikang Vein-type Pb-Zn-Ag-Sb Deposit in Himalayan Orogen, Tibet: Product by Overprinting and Remobilization Processes during Post-collisional Period

LIANG Wei<sup>1, \*</sup>, HOU Zengqian<sup>2</sup>, ZHENG Yuanchuan<sup>3</sup>, YANG Zhusen<sup>4</sup> and LI Zhenqing<sup>4</sup>

<sup>1</sup> Chengdu Center, China Geological Survey, Chengdu 610082, China

<sup>2</sup> Institute of Geology, Chinese Academy of Geological Sciences, Beijing 100037, China

<sup>3</sup> China university of geosciences, Beijing 100037, China

<sup>4</sup> Institute of Mineral Resources, Chinese Academy of Geological Sciences, Beijing 100037, China

**Abstract:** The Zhaxikang Pb-Zn-Ag-Sb deposit, the largest polymetallic deposit known in the Himalayan Orogen of southern Tibet, is characterized by vein-type mineralization that hosts multiple mineral assemblages and complicated metal associations. The deposit consists of at least six steeply dipping vein-type orebodies that are hosted by Early Jurassic black carbonaceous slates and are controlled by a Cenozoic N-S-striking normal fault system. This deposit records multiple stages of mineralization that include an early period (A) of massive coarse-grained galena-sphalerite deposition and a later period (B) of Sb-bearing vein-type mineralization. Period A is only associated with galena-sphalerite mineralization, whereas period B can be subdivided into ferrous rhodochrosite-sphalerite-pyrite, quartz-sulfosalt-sphalerite, calcite-pyrite, quartz-stibnite, and quartz-only stages of mineralization. The formation of brecciated galena and sphalerite ores during period A implies reworking of pre-existing Pb-Zn sulfides by Cenozoic tectonic deformation, whereas period B mineralization records extensive open-space filling during ore formation. Fluid inclusion microthermometric data indicate that both periods A and B were associated with low-medium temperature (187–267°C) and low salinity (4.00–10.18% wt. NaCl equivalent) ore-forming fluids, although variations in the physical-chemical nature of the period B fluids suggest that this phase of mineralization was characterized by variable water/rock ratios. Microprobe analyses indicate that Fe concentrations in sphalerite decrease from period A to period B, and can be divided into three groups with FeS concentrations of 8.999–9.577, 7.125–9.109, 5.438–1.460 mol.%. The concentrations of Zn, Sb, Pb, and Ag within orebodies in the study area are normally distributed in both lateral and vertical directions, and Pb, Sb, and/or Ag concentrations are positive correlation within the central part of these orebodies, but negatively correlate in the margins. Sulfide S isotope compositions are highly variable (4‰–13‰), varying from 4‰ to 11‰ in period A and 10‰ to 13‰ in period B. The Pb isotope within these samples is highly radiogenic and defines linear trends in  $^{206}\text{Pb}/^{204}\text{Pb}$  vs.  $^{207}\text{Pb}/^{204}\text{Pb}$  and  $^{206}\text{Pb}/^{204}\text{Pb}$  vs.  $^{208}\text{Pb}/^{204}\text{Pb}$  diagrams, respectively. The S and Pb isotopic characteristics indicate that the period B orebodies formed by mixing of Pb-Zn sulfides and regional Sb-bearing fluids. These features are indicative of overprinting and remobilization of pre-existing Pb-Zn sulfides by Sb-bearing ore-forming fluids during a post-collisional period of the Himalayan Orogeny. The presence of similar ore types in the north Rhenish Massif that formed after the Variscan Orogeny suggests that Zhaxikang-style mineralization may be present in other orogenic belts, suggesting that this deposit may guide Pb-Zn exploration in these areas.

**Key words:** polymetallic, multiple period and stage mineralization, overprinting and remobilization, orogenic belt, Zhaxikang, Tibet

\* Corresponding author. E-mail: lwcugb@126.com

## 1 Introduction

The Himalaya orogen-related Sb-Au-Pb-Zn polymetallic belt of southern Tibet is a poorly known but highly prospective metallogenic belt (Yang Zhusen et al., 2006; Hou and Zhang et al., 2015). The mineral deposits within this belt are thought to relate to the formation of the south Tibetan detachment system (STDS) during Indo-Asian collision (Nie Fengjun et al., 2005; Yang et al., 2009). At least fifty Sb, Sb-Au, and Au deposits and occurrences have been found in this belt (Yang et al., 2009; Zhai et al., 2014). These deposits occur along or are associated with a series of E–W-striking structural–thermal domes. Recent mineral exploration has discovered several Pb–Zn–(Ag) deposits (Qi Xuexiang et al., 2008) that are associated with Sb mineralization and sporadically occur on the southern side of the domed area. The metallogenic belt has a broad metallogenic zoning that varies from southernmost Pb–Zn mineralization to central Sb–Pb–Zn and northern Sb–Au associations (Fig. 1). The formation of the mineralization within the Himalayan Sb–Au–Pb–Zn belt is poorly understood, especially when compared with other metallogenic belts within the Tibetan–Himalayan orogen.

The Zhaxikang deposit (Fig. 1b) is the largest known Sb and Pb–Zn–Ag mineralized deposit in the Himalayan Sb–Au–Pb–Zn belt (Fig. 1b; Liang Wei et al., 2013), and was

discovered in the 1990s. The Zhaxikang has been a suitable window to understand the metallogensis of Himalayan Sb–Au–Pb–Zn belt, therefore several studies has been done for geology, ore fluid and oregensis, respectively. Meng Xiangjin et al. (2008) suggested those quartz–stibnite veins at Zhaxikang were related to hot-spring processes by studying Si–O–H isotopes. Zhu Likuan et al. (2012) thought that fluid of Zhaxikang is a medium–low temperature, low salinity, low density H<sub>2</sub>O–NaCl system formed during groundwater convection cycle driven by sedimentary–structural–geothermal activity, while Xie et al. (2017) argued that Zhaxikang veins are related to magmatic activities based on detailed fluid inclusion study, which was consistent with sulfur isotopic research by Yang et al. (2009) and also with Zn–Pb isotopes of galena, sphalerite, and Mn–Fe carbonate studies by Duan et al. (2017). Some researchers proposed that Zhaxikang ores underwent multiple mineralization events (Liang Wei et al., 2013; Wang et al., 2017; Sun et al., 2018; Zhou et al., 2017). Obviously, there are different opinions on oregensis of Zhaxikang for its complicated and multiple mineralization events (Zheng Youye et al., 2014; Liang Wei et al. 2013; Wang et al. 2017; Sun et al., 2018), and the ore-forming process of Zhaxikang needs to be further discussed.

Discovered in the 1990s, the ongoing exploration and mining identified the presence of a polymetallic but Pb–Zn

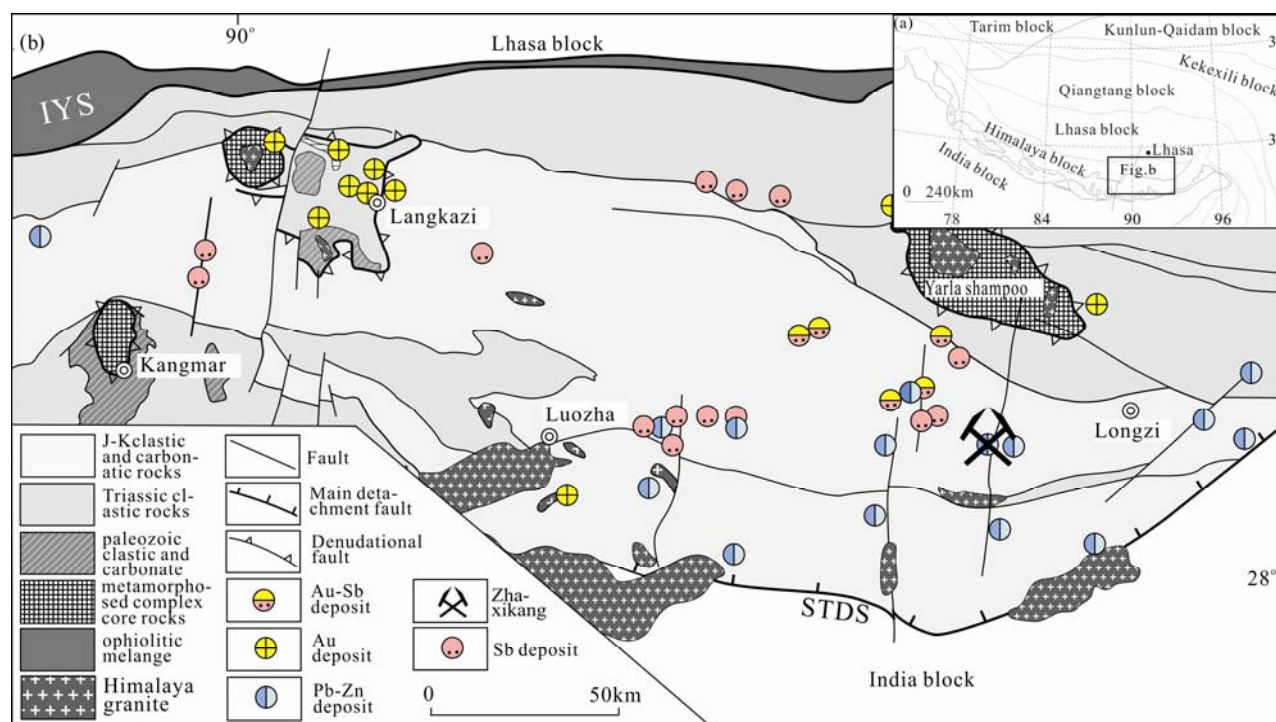


Fig. 1. Simplified geological map of the eastern Tethyan Himalaya showing the tectonic framework of the Tibetan orogenic belt and the distribution of antimony–gold deposits, thermal domes, and leucogranites in southern Tibet; adapted from Yang et al. (2009).

(a), Tectonic framework of the Tibetan orogenic belt; (b), Location of the Zhaxikang polymetallic deposit in the antimony–gold metallogenic belt within the study area.

-dominated deposit in Zhaxikang, which also contains significant amounts of Ag and Sb mineralization, and in 2012 had reserves of 445,000 tons of Pb, 823,000 tons of Zn, 138,000 tons of Sb and 1,799 tons of Ag (Zhang Jianfang et al., 2012). Recent exploration has expanded these reserves and the deposit is now known to contain 15.92 Mt of ore reserves and 1.47 Mt of contained metal, which makes the Zhaxikang deposit the only large polymetallic deposit within the Tethyan Himalayan metallogenic belt (THMB; Zheng Youye et al., 2012); all other deposits in this area are currently classified as small or medium in size. The ores within the Zhaxikang deposit are vertically zoned, from upper Sb orebodies to lower Pb-Zn-Ag orebodies, similar to vein deposits within the Rheinisches Schiefergebirge district, which is located in a post-Variscan orogenic belt in western Germany (Wagner and Cook, 1998). However, it is still unclear why the Pb-Zn mineralization in this area is closely associated with Sb mineralization; for example, is this association merely coincidence or is it a result of some regional mineralizing event associated with collisional orogenesis. Here, we describe the geology and mineralization within the Zhaxikang deposit with presenting S-Pb isotopes and elements ratios, Fe/Zn relationship of minerals to discuss the overprinting-remobilization processes that formed the deposit and their implications for mineral exploration.

## 2 Regional Geology

The Tibetan-Himalayan orogenic system formed as a result of the early Tertiary Indo-Asian continental collision, and consists of a collage of E-W-striking terranes or blocks (Harrison et al., 1992; Yin and Harrison, 2000); these are, from north to south, the Qiangtang, Lhasa, and Himalayan terranes. These terranes are separated by the Bangonghu-Nujiang Suture (BNS) and Indo-Yarlung Zangpo Suture (IYS) (Fig. 1b), and the main boundary between the Indian and Asian continents is marked by the IYS (Searle et al., 1987; Yin and Harrison, 2000; Leech et al., 2005; Mulch and Chamberlain, 2006), which formed as a result of northward subduction of Neo-Tethyan oceanic lithosphere during the Cretaceous (Kapp et al., 2005). This boundary is crosscut by a south-dipping thrust system that contains at least five south-dipping thrust faults along the entirety of the IYS (Yin and Harrison, 2000). The Himalaya Terrane (Fig. 1b) is bounded by the IYS and the Main Frontal thrust (MFT), and consists of four lithotectonic units (from north to south): the Tethyan Himalaya (TH), the Greater Himalaya (GH), the Lesser Himalaya (LH), and the Sub-Himalaya (SH; Hodges, 2000; Yin and Harrison, 2000). These four

units are separated by three east-west trending and north-dipping Cenozoic fault systems, including, from north to south, the South Tibetan detachment system (STDS), the Main Central thrust (MCT), and the Main Boundary thrust (MBT; Fig. 1b). The Tethyan Himalaya represents a passive continental margin of the Indian continent, and consists of late Precambrian to early Paleozoic crystalline basement rocks and Permian to Late Cretaceous marine sedimentary sequences (Burchfiel et al., 1992) as well as widespread bimodal volcanics (Zhu et al., 2008; Lv et al., 2016). A number of mafic dykes intruded into these basement rocks and sedimentary rocks (Kumar et al., 2016; Wang Yaying et al. 2016). The central part of the Tethyan Himalaya is dominated by a sequence of Jurassic-Cretaceous deep to shallow marine shales and sandstones (Fig. 1b). Several thermal domes (e.g., the Yarlashampoo, Lhagoi Kangri, Kangmar, and Compa domes) form a >1000 km belt within the central Tethyan Himalaya, and is one of the more unusual characteristics of this area (Burchfiel, 1992; Hauck et al., 1998; Lee et al., 2000, 2004; Quigley et al., 2006; Zeng Lingsen et al., 2009). The majority of these domes have cores that consist of Paleozoic and Neoproterozoic augen orthogenesis and/or paragenesis (Debon et al., 1986; Gao Hongxue et al., 1996), surrounded by progressively less metamorphosed Carboniferous-Triassic sedimentary sequences (Burg et al., 1984; Schärer et al., 1986; Harrison et al., 1997; Lee et al., 2004). These domes are commonly intruded by Cenozoic 17.6–9.5 Ma leucogranites (Burchfiel, 1992; Harrison et al., 1997; Burg et al., 1984; Debon et al., 1986; Hu Guyue et al., 2016), indicating that the domes formed at 18–13.5 Ma (Liu Wencan et al., 2004; Quigley et al., 2006; Zhang Jinjiang et al., 2012). The leucogranites are thought to have formed during melting of upper crustal metapelites and were intruded into or around these domes along low-angle faults and/or fractures (Harris and Massey, 1994; Guillot and Le Fort, 1995; Searle et al., 1997).

Another important tectonic event in the study area is mid-Miocene E-W extension (Molnar and Tapponnier, 1978; Armijo et al., 1986; England and Houseman, 1989; Harrison et al., 1992; Yin et al., 1999; Yin and Harrison, 2000), which formed a series of north-south-trending rift systems (e.g. the Yadong-Yangbajing-Gulu graben; Cogan et al., 1998) that are bounded by moderate- to high-angle normal faults (Tapponnier and Molnar, 1977; Molnar et al., 1978; Pan and Kidd, 1992; Harrison et al., 1995; Blisniuk et al., 2001). Movement along these normal fault systems was diachronous, but generally occurred at 18–4 Ma (Maluski et al., 1988; Pan and Kidd, 1992; Coleman and Hodges, 1995; Yin et al., 1999; Blisniuk et al., 2001). In addition, N-S-striking normal faults that effectively

control the location of post-collisional mineralization (Hou Zengqian et al., 2006; Hou and Cook, 2009; Yang et al., 2009), and also control the location of the southern Tibetan antimony–gold ore systems (Yang et al., 2009), including the Zhaxikang deposit (Yang et al., 2009; Qi Xuexiang et al., 2008).

### 3 Deposit Geology

#### 3.1 Stratigraphy and structure

The Zhaxikang deposit is hosted by Jurassic argillaceous and siliciclastic sedimentary rocks ( $J_1r$ ,  $J_3w$ ; Fig. 2), and the majority of mineralization within the deposit is hosted by the Ridang Formation ( $J_1r$ ), a sequence of bedded dark gray to grayish black shales, argillaceous and calcareous shales, sandstones containing minor tuff, and conglomeratic cherts. This formation can be divided into four units (Fig. 2a): a yellowish brown coarse-grained quartz sandstone unit ( $J_1r^1$ ), a black shale ( $J_1r^2$ ), a celadonite-bearing quartz sandstone unit ( $J_1r^3$ ), a carbonaceous slate unit ( $J_1r^4$ ), and a quartz sandstone and shale unit ( $J_1r^5$ ). The other main sedimentary sequence in

the study area is the Weimei Formation ( $J_3w$ ), which consists of lowermost quartz sandstone and uppermost metasandstone units; the area also contains minor amounts of hot spring sediments located in and around the mine.

The study area is characterized by a series of N–S- and NNE–SSW-striking normal faults that control the spatial location of mineralization within the Zhaxikang deposit (Fig. 2a, b). More than 10 of these fault systems have been recognized, almost all of which record sinistral strike-slip movements and dip steeply ( $60^\circ$ – $80^\circ$ ) to the west. Fracture zones along these normal faults are filled by breccias with clasts of different sizes; this brecciation also generated open spaces that were filled by ore minerals during deposit formation. The most important faults in the study area are faults F7 and F2, which control the location of the most important orebodies (e.g., the V and VI orebodies; Fig. 2b). F2 is located to the north of the orefield, has a length of >1300 m, is 1–12 m wide, has an S-shaped surface expression, and dips to the west at about  $60^\circ$ . F7 is located to the west of F2 (Fig. 2b), has a length of >1000 m, and branches out into smaller faults at depth. This fault records multiple stages of tectonism, and has a width of ~1–30 m, strikes nearly N–S and dips at  $45^\circ$ – $70^\circ$  to the west and is filled by unshaped breccias containing clasts that vary in size from ~2 cm to 20 m or larger.

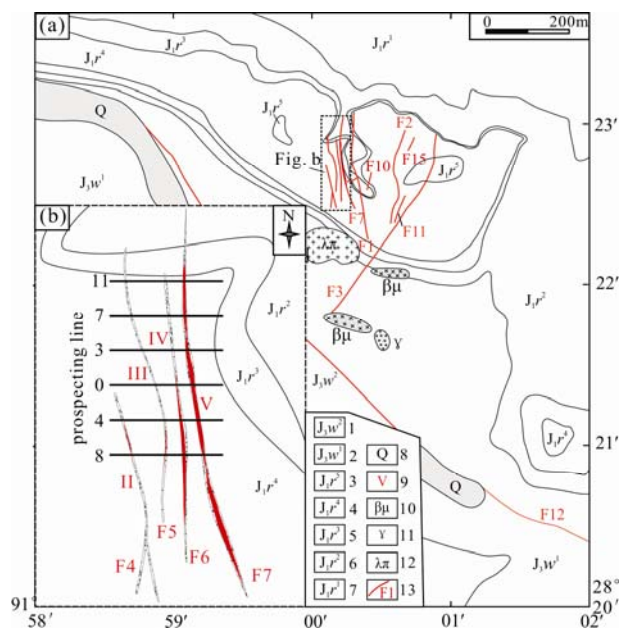


Fig. 2. Geological map of the Zhaxikang Pb-Zn-Ag-Sb polymetallic deposit; modified from a detailed exploration report by Huayu Ltd. Co. (2009).

(a), ore-veins are mainly hosted by Jurassic carbonaceous slates, and is controlled by N–S-striking normal faults. The map shows details of the geology, the location of igneous rocks, and tectonic features of the area; (b), Inset shows details of the location of orebodies VI and V orebodies. Numbers within legend: 1, metasandstone of Weimei Formation 2nd Segment; 2, quartz-sandstone of Weimei Formation 1st Segment; 3, quartz-sandstone and shale of Ridang Formation 5th Segment; 4, carbonaceous slate of Ridang Formation 4th Segment; 5, celadon quartz sandstone of Ridang Formation 3rd Segment; 6, black shale of Ridang Formation 2nd Segment; 7, yellowish-brown coarsed quartz sandstone of Ridang Formation 1st Segment; 8, the quaternary sediments; 9, numbers of ore veins; 10, diabase dykes; 11, muscovite granite porphyry; 12, rhyolite porphyry; 13, faults.

#### 3.2 Igneous rocks

A ~2 km<sup>2</sup> Cretaceous porphyritic rhyolite stock (Zhang Jianfang et al., 2010) outcrops to the west of the mining area (Fig. 2a), and contains small K-feldspar and quartz phenocrysts in a glassy matrix. The hypabyssal rocks in the area are porphyritic and have rhyotaxitic structures, and the south of the study area contains diabase dikes and granitic stocks. The diabase is typically ophitic, and consists of pyroxene and plagioclase with minor amphibole and K-feldspar. The porphyritic granitic stocks contain quartz and K-feldspar phenocrysts in a fine-grained quartz and/or glassy matrix (Zhang Jianfang et al., 2010).

### 4 Mineralization and Alteration

#### 4.1 Orebodies

At least six orebodies have been recognized in the studied area, all of which are controlled by N–S and NNE–SSW-striking normal faults (Table 1). The I, II, and III orebodies contain minor amounts of Pb and/or Sb mineralization, and are associated with the F1, F4, and F5 faults, respectively. These orebodies contain mineralization that is confined to fracture zones, and contain relatively low grade of sulfides that incompletely fill spaces within the fault breccias. Although these faults

**Table 1 Characteristics of orebodies within the study area**

ore bodies	controlled fault	stratigraphy	attitudes	fault length	mineralization	alteration
I	F1	$J_1r^2, J_1r^3, J_1r^4$	nearly NS-striking	1400 m	poor sb and pb	ferritization, pyritization silicification
II	F4	$J_1r^4$	nearly NS-striking	520 m	poor sb	ferritization, pyritization silicification, hloritization calcitization
III	F5	$J_1r^2, J_1r^3, J_1r^5$	nearly NS-striking	450 m	rich in sb and pb	ferritization, clayzation, silicification
IV	F6	$J_1r^4$	west-dipping at 55°	470 m	rich in sb and pb	ferritization, pyritization, silicification, calcitization, chloritization
V	F7	$J_1r^4$	west-dipping at 45–70°	1000 m	rich in pb-zn-ag-sb	ferritization, pyritization silicification, calcitization chloritization,sericization
VI	F2	$J_1r^4$ and $J_1r^5$	nearly NS-striking	1300 m	rich in pb and zn	ferritization, silicification pyritization

extend for hundreds of meters (Table 1), the orebodies associated with these faults are small, with widths of 1–7 m, lengths of 10–50 m, and maximum depths of 100 m.

The IV, V, and VI orebodies are the main hosts of mineralization within the Zhaxikang deposit. All of these orebodies dip to the west at 45°–80° and strike nearly N–S (Table 1). The IV orevein is located in F6, which is irregular shaped and lenticular with an average grade of Pb (3.66%), Zn (9.20%). The VI orebody is controlled by F2, which extends 600 meters long on surface with an average thickness of 6.35 meters and grade of Pb (0.29%), Zn (2.27%), Sb (1.05%) and Ag (48.48g/t). The V orebody is the most important of these orebodies with an average grade of Pb (1.99%), Zn (2.85%), Sb (1.16%) and Ag (87.18 g/t), as it is the largest and highest-grade orebody within the deposit, and is both laterally and vertically zoned. This orebody outcrops over a surface area of ~50 m, but the majority of the orebody is located at depth along the west-dipping F7 (Fig. 3) and dips to the north (Fig. 4a). The width of the orebody ranges from ~1.5 to ~30 m, but averages about 8 m, and the orebody increases in width and length with depth, but splits into branches in the deeper parts of the orebody (as observed in mining adits (MA) at depth; Fig. 4b). The orebody is

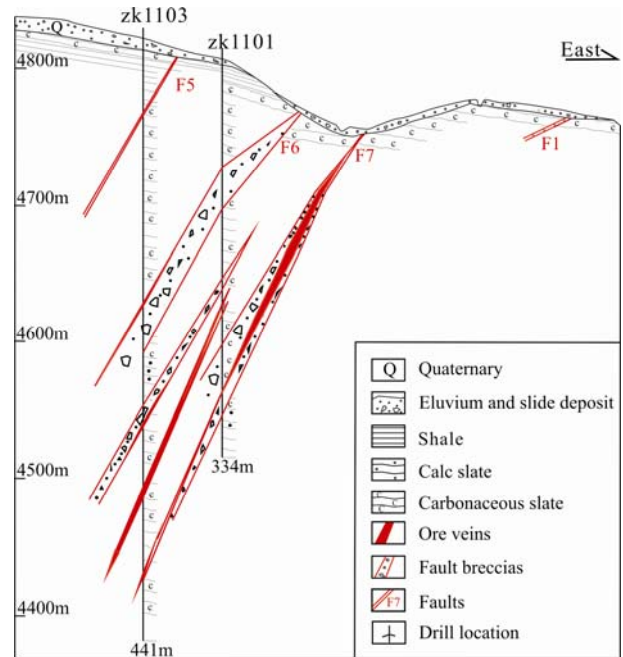


Fig. 3. Cross-section along prospecting line 11 cross section (shown in the bottom left of Fig. 2) showing the vertical distribution mineralization within orebody V. Mineralized veins originate in moderate to high angle normal faults, and the F7 fault hosts the highest grade mineralization; modified from a detailed exploration report by Huayu Ltd. Co. (2009).

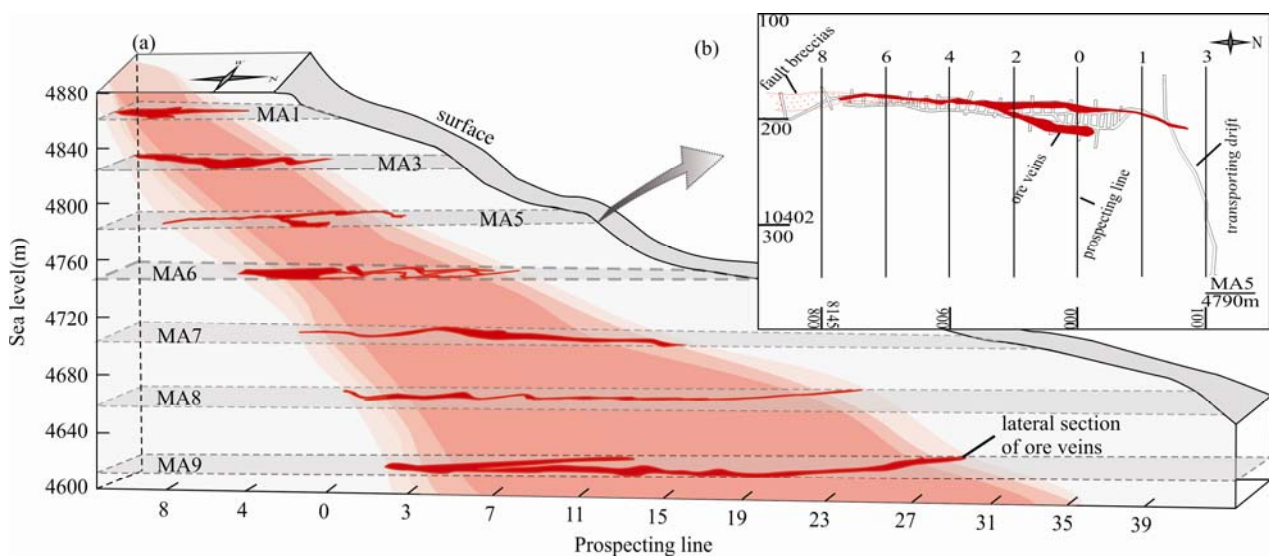


Fig. 4. Morphology of the highest grade and largest orebody within the deposit (V).

(a), 3D model of orebody V based on the presence of mining adits (MA) at different heights within the deposit and prospecting lines; (b), Plan view of MA5 showing the lateral distribution of mineralization; modified from a detailed exploration report by Huayu Ltd. Co. (2009).

vertically zoned from a lowermost sphalerite + galena assemblage through sphalerite + sulfosalt mineral and sphalerite+stibnite zones to an uppermost stibnite zone of mineralization. The gangue minerals within the orebody also vary from a lowermost Fe-Mn carbonate + pyrite gangue through Fe-Mn carbonate + pyrite + arsenopyrite + quartz, and calcite + pyrite + quartz assemblages to an uppermost quartz gangue. Lateral variations are evidenced by variations from the core to the margins of the orebody, with a central galena + sphalerite zone giving way to sphalerite + sulfosalt mineral and sphalerite + stibnite zones to a marginal stibnite zone.

The Zhaxikang deposit has undergone only weak hydrothermal alteration, and this alteration is not zoned. Alteration within the deposit includes silicification, and iron, pyrite, calcite, chlorite, and sericite alteration, all of which is preferentially developed within and around normal faults. Silicification is generally related to areas of Sb-bearing mineralization, which occur as meuliere masses, quartz veins, and clusters in open spaces within faults (Fig. 6g2, g3, i1). Iron alteration is associated with surficial exposures of mineralization and is an important indicator of Pb-Zn mineralization (Fig. 6a3), although some Fe alteration is also associated with fracture zones (Fig. 7). Pyrite alteration is associated with fracture zones along the fault system (Fig. 6f1, f2), is also widespread in Jurassic carbonaceous slates (Fig. 6f1), and is closely related to Pb-Zn-Ag mineralization (Fig. 6a1). Calcite alteration is locally associated with pyrite alteration around individual orebodies (Fig. 6f1, f2), and chlorite, sericite, and clay alteration are relatively weakly developed in scattered parts of the upper sections of the main orebodies. In addition to these main types of alteration, weathering and oxidation have affected orebodies exposed at the surface, forming minerals such as anglesite (Ang), malachite (Mal), and azurite (Azu) (Fig. 6i2; Fig. 7b).

#### 4.2 Mineral Assemblages and ore structures

The mineralogy of the Zhaxikang deposit is dominated by galena, sphalerite, sulfosalt minerals (i.e., boulangerite, jamesonite, freibergite, tetrahedrite, and zinkenite), and stibnite, in a gangue that contains quartz, rhodochrosite, arsenopyrite, pyrite, siderite with minor chalcopyrite, covellite, calcite, malachite, anglesite, and chalcedony.

There are two main types of ore within the deposit: (i) brecciated and massive ores (Fig. 6a) that contain Pb-Zn minerals without Sb, and (ii) open-space filling ores that form banded, crustiform, comb, drusy, and cavity-filling mineralization that is associated with Sb-bearing minerals. These ores have various textures, including coarse- and fine-grained ores, anhedral to euhedral ores, embayed,

enclosed, and replacement textures. This is exemplified by the V orebody, where ore textures change regularly from the top to the bottom of the orebody, with upper veinlet ores giving way to stockwork, cavity, and coarse vein types of mineralization at depth, and disseminated and crustiform ores changing to brecciated and massive ores with increasing depth. The textures within the orebody also vary systematically, with lowermost coarse-grained and semi-idiomorphic granular ores changing to fine-grained idiomorphic allotriomorphic granular ores, and an uppermost series of idiomorphic ores.

#### 4.3 Stages of mineralization

The crosscutting relationships of veins and mineral assemblages within the deposit enable the formation of the deposit to be split into 2 periods, 6 stages, and 12 substages (Fig. 5). The different periods of mineralization are defined by the formation of mineralization at different times, whereas stages are defined according to the crosscutting relationships of the main ore veins within a period, and substages are defined by the order of mineral precipitation within a stage. The mineralization periods, stages and substages are named as A(I,1) for period, stage and substage, respectively.

##### 4.3.1 Massive coarse-grained galena-sphalerite mineralization period (A)

Only galena and sphalerite were deposited during this period of mineralization and are associated with a pyrite and rhodochrosite gangue. This period is associated with coarse-grained ore veins that transition into breccias that are surrounded and/or crosscut by later ore veins, indicating that this period was the earliest stage of mineralization. Period A only includes a galena-sphalerite stage of mineralization.

**Galena-sphalerite stage A (I, 1):** This stage of mineralization is associated with quartz-free ores containing coarse-grained galena (40%–45%), sphalerite (25%–30%), pyrite (5%–10%), and rhodochrosite (10%–15%) (Fig. 5). These ores are generally massive, lens-shaped, or brecciated (Fig. 6a, b), although successive mineral veins are rarely located within fracture zones (Fig. 6a2). The rhodochrosite and pyrite gangue (Fig. 6b) was coprecipitated with galena and sphalerite (Fig. 6a1), and the Pb/Zn ratio of the mineralization that formed during this stage changes from orebody to orebody (e.g., the VI orebody contains more Pb than Zn, but the V orebody contains less Pb than Zn).

The only Pb-bearing mineral formed during period A is coarse-grained galena, which is generally massive, lens-shaped, and brecciated but is only rarely present in veins (Fig. 6a2, a3). This galena also records extrusion lineation

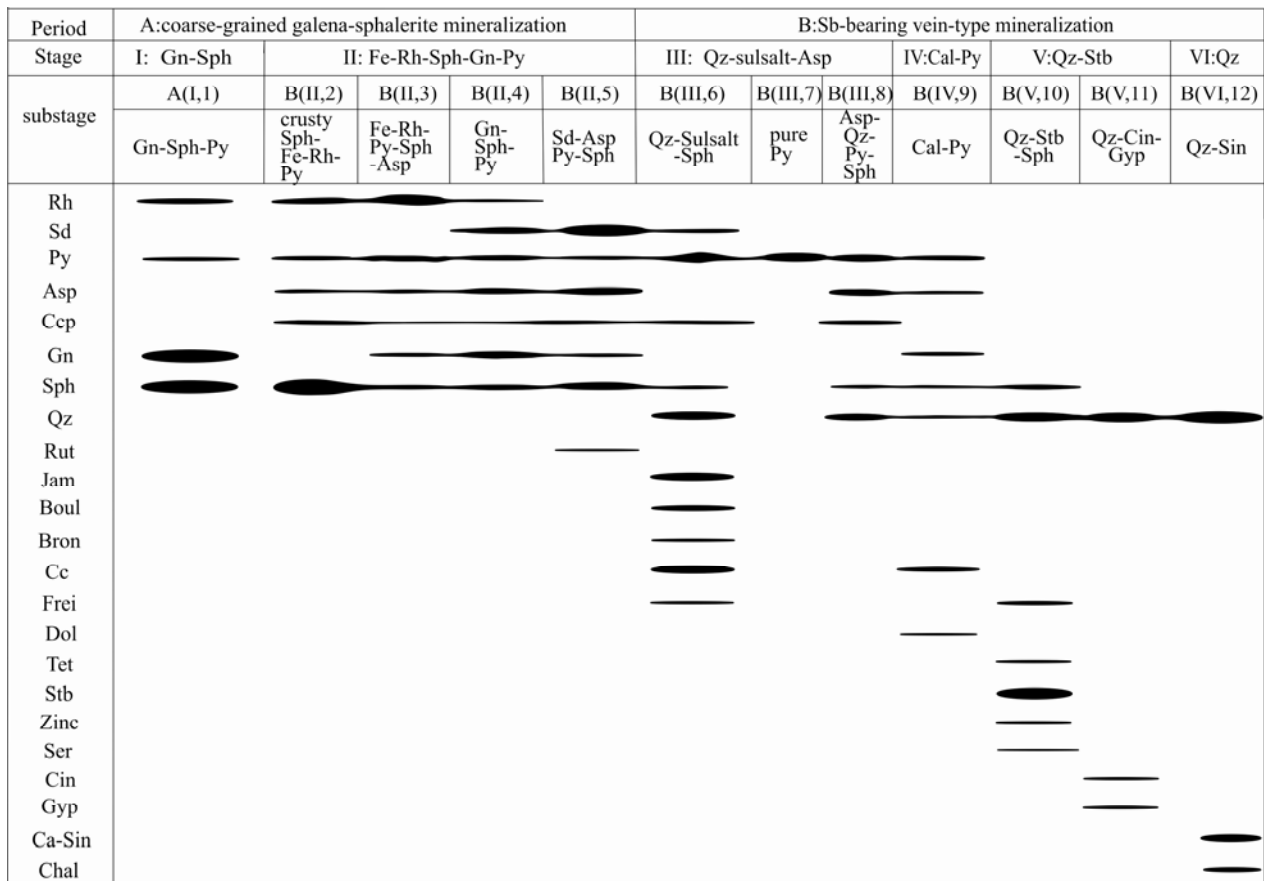


Fig. 5. Paragenesis of mineralization within the polymetallic Zhaxikang Pb-Zn-Ag-Sb deposit showing the formation of different mineral assemblages during each period of mineralization.

Abbreviations are as follows: Fe-Rh, ferrous rhodochrosite; Sd, siderite; Py, pyrite; Asp, arsenopyrite; Ccp, chalcopryrite; Gn, galena; Sulsalt, sulfosalts; Sph, sphalerite; Qz, quartz; Dol, dolomite; Cc, calcite; Rut, rutile; Jam, jamesonite; Boul, boulangerite; Bron, bronngniardite; Frei, freibergite; Tet, tetrahdrite; Stb, stibnite; Zinc, zinkenite; Ser, sericite; Cin, cinnabar; Gyp, gypsum; Ca-Sin, calc-sinter; Chal, chalcedony.

related to compressional stress (Fig. 6a4), which is also visible as the preferential orientation of triangular polishing pits within galena (Fig. 6a1).

Period A sphalerite has similar structures and textures to the galena formed during this period, is coarse-grained, and is present as massive and brecciated ore that is commonly surrounded by later-formed pyrite and ferrous rhodochrosite (Fig. 6b2). The sphalerite that formed during this period is dark black because of high Fe concentrations. In addition, the coarse-grained sphalerite and galena breccias within the orebodies have no identifiable precursor sphalerite-galena veins.

#### 4.3.2 Sb-bearing vein mineralization period (B)

Period B is characterized by the formation of significant amounts of Sb-bearing minerals, including sulfosalt minerals and stibnite, as well as ore veins; given this, this period is termed the Sb-bearing vein mineralization period. Five stages (Fig. 5) of mineralization have been identified during this period: the ferrous rhodochrosite-sphalerite-galena-pyrite, quartz-sulfosalt-arsenopyrite, calcite-pyrite, quartz-stibnite, and quartz stages.

#### (I) Ferrous rhodochrosite-sphalerite-galena-pyrite stage B (II)

This stage is characterized by the formation of medium- to fine-grained sphalerite and galena in crustiform to veinlet-type structures associated with ferrous rhodochrosite and pyrite gangue that also contains rare arsenopyrite. Stage II consists of 4 substages that are characterized by the formation of crustiform sphalerite-ferrous rhodochrosite-pyrite, ferrous rhodochrosite-pyrite-sphalerite-arsenopyrite, galena-sphalerite-pyrite, and siderite-arsenopyrite-pyrite-sphalerite assemblages.

**Crustiform sphalerite-ferrous rhodochrosite-pyrite substage B (II, 2):** This substage is characterized by the formation of medium-grained crustiform and massive ores that contain sphalerite (35%–45%), ferrous rhodochrosite (30%–40%), pyrite (5%–10%), chalcopryrite (<5%), and minor arsenopyrite (<1%; Fig. 5). The sphalerite is intergrown with pyrite and ferrous rhodochrosite around brecciated stage I sphalerite (Fig. 6b2, b3). Both simple and complex sphalerite crusts (Fig. 6c) vary in width from 0.5 to 3 cm, and this stage marks the appearance of chalcopryrite droplets (i.e., chalcopryrite disease; <5%) in



Fig. 6. Images of typical features of the minerals, structures, and textures of each stage of mineralization within the Zhaxikang deposit.

(a), Coarse galena vein formed during period A: a1, Coarse-grained galena intergrown with sphalerite and pyrite; a2, Vein-hosted coarse-grained galena in carbonaceous slate; a3, Vein-hosted coarse-grained galena in hand specimen, showing intense oxidation; a4, compressional lineation within coarse-grained brecciated galena; (b), Contact relationship between sphalerites formed during period A and B: b1, Brecciated sphalerite and rhodochrosite cemented by Fe-rhodochrosite; b2, Crustiform sphalerite-Fe-rhodochrosite; (c), Complex crustiform sphalerite-Fe-rhodochrosite crosscut by later stage quartz-sulfosalt-sphalerite vein; (d), Fine-grained galena + sphalerite + Fe-rhodochrosite + arsenopyrite mineralization crosscutting a Fe-rhodochrosite + sphalerite + pyrite vein, and being crosscut by a quartz + sulfosalt + sphalerite vein; (e), Paragenesis of mineralization in the study area: Fe-rhodochrosite + sphalerite + pyrite + arsenopyrite vein  $\rightarrow$  siderite + arsenopyrite + pyrite + sphalerite vein  $\rightarrow$  quartz + sulfosalts + sphalerite  $\rightarrow$  pure pyrite  $\rightarrow$  arsenopyrite + quartz + pyrite + sphalerite veinlet; (f), Pyrite + calcite + dolomite substage: f1, Calcite and pyrite within carbonaceous slate; f2, Beige dolomite in calcite vein; (g), Quartz-sinter stage of mineralization: g1, calcite-dominated sinter to the west of Zhaxikang; g2, Idiomorphic finger-like quartz growths on the outside of a quartz-stibnite breccia; g3, Barren hot spring-type quartz; (h), Calcite + pyrite substage of mineralization associated with porphyritic sericite and very small sphalerite; (i), i1, Later period barren quartz vein without mineralization; i2, Malachite and azurite formed during the supergene period of mineralization; Mal, malachite; Azu, azurite.

sphalerite.

**Ferrous rhodochrosite-pyrite-sphalerite-arsenopyrite substage B (II, 3):** This substage is characterized by medium-grained vein and crustiform ferrous rhodochrosite (30%–40%), pyrite (20%–30%), sphalerite (10%–15%), arsenopyrite (5%–10%), chalcopyrite (<5%) and minor rutile (<<1%; Fig. 5). This substage is associated with the formation of significant amounts of pyrite and arsenopyrite (Fig. 6d, e), and intergrown ferrous

rhodochrosite, pyrite, and arsenopyrite (Fig. 8f) that is absent from mineralization formed during the *crustiform sphalerite-ferrous rhodochrosite-pyrite* substage. Minor rutile is associated with the ferrous rhodochrosite formed during this substage, and chalcopyrite inclusions are still present in sphalerite.

**Galena-sphalerite-pyrite substage B (II, 4):** This substage is characterized by fine-grained galena (15%–20%), sphalerite (15%–20%), pyrite (20%–25%),

arsenopyrite (5%–10%), Mn-bearing siderite (10%–15%), and chalcopyrite (<10%) veinlets (Fig. 5). The chalcopyrite that formed during this substage is present as inclusions within sphalerite or as short veins that also contain galena and sphalerite. This substage crosscuts the ferrous rhodochrosite–pyrite–sphalerite–arsenopyrite substage along the 5<sup>th</sup> prospecting line within the 4620 section of orebody V (Fig. 6d).

**Siderite-arsenopyrite-pyrite-sphalerite substage B (II, 5):** This substage is associated with a siderite (30%–35%), arsenopyrite (20%–25%), pyrite (10%–15%), sphalerite (15%–20%), and chalcopyrite (<5%) assemblage (Fig. 5) that is dominated by pale yellow siderite that coexists with chalcopyrite-bearing sphalerite. Arsenopyrite and pyrite are present along the boundaries of siderite veinlets, and siderite–arsenopyrite–pyrite–sphalerite veins crosscut galena–sphalerite–pyrite mineralization, and in turn are crosscut by quartz–sulfosalt–arsenopyrite stage mineralization along the 7<sup>th</sup> prospecting line within orebody V (Fig. 6e).

### (2) Quartz-sulfosalt-arsenopyrite stage B (III)

This stage of mineralization is associated with the deposition of quartz, calcite, sphalerite, stibnite, arsenopyrite, and various sulfosalt minerals with minor pyrite and chalcopyrite in open-space filling ores that are present as stockworks, druses, and cavities, are subhedral

to euhedral, and have replacement textures. The veins that formed during this stage have widths of <10 to ~50 cm. The sulfosalt minerals that formed during this stage of mineralization include boulangerite, jamesonite, brongniardite, and freibergite, and are important Sb-bearing minerals that are also present in other deposits within the TH Sb–Au–Pb–Zn belt. Jamesonite and boulangerite are the most abundant sulfosalt minerals associated with this stage of mineralization, and this stage is associated with higher abundances of arsenopyrite than any other within the deposit. This stage is divided into quartz–sulfosalt–sphalerite, pure pyrite, and arsenopyrite–quartz–pyrite–sphalerite substages.

**Quartz-sulfosalt-sphalerite substage B (III, 6):** The mineralization that formed during this substage is present as euhedral to subhedral mineralization in druses, cavities, and stockworks. The ore veins that formed during this substage crosscut the carbonaceous slate wallrock and mineralization formed during previous stages (Fig. 6d, e). This mineralization contains quartz (30%–35%), sphalerite (10%–15%), jamesonite (10%–15%), boulangerite (10%–15%), brongniardite (<5%), freibergite (<5%), pyrite (<5%), and chalcopyrite (5%; Fig. 5), and contains sphalerite with abundant droplet-like chalcopyrite (Fig. 8e) in quartz–sulfosalt veins. Sulfosalt minerals rich in Pb, Sb, and/or Ag fill spaces within euhedral quartz grains (Fig. 8c), and needle- and hair-like sulfosalt minerals and quartz are also present within geodes. The quartz–sulfosalt–sphalerite substage of mineralization crosscuts the siderite–arsenopyrite–pyrite–sphalerite substage, but is itself cut by later pure pyrite substage mineralization along the 7<sup>th</sup> prospecting line within orebody V (Fig. 6e).

**Pure pyrite substage B (III, 7):** This substage is associated with fine-grained pyrite veins that have widths of 1–3 cm and crosscut earlier quartz–sulfosalt–sphalerite substage mineralization (Fig. 6e).

**Arsenopyrite-quartz-pyrite-sphalerite substage B (III, 8):** This substage of mineralization is associated with arsenopyrite (30%–35%), quartz (15%–20%), pyrite (20%–25%), sphalerite (10%–15%), and chalcopyrite (<5%; Fig. 5), with numerous fine-grained arsenopyrite veinlets and stockworks associated with light-brown fine-grained chalcopyrite-bearing sphalerite.

### (3) Calcite-pyrite stage B (IV, 9)

The subhedral to xenomorphic textured mineralization that formed during this stage is hosted by large veins (Fig. 6f1, f2) and consists of calcite (50%–55%) and pyrite (20%–30%) associated with dolomite (~10%), quartz (<5%), and sphalerite (<1%; Fig. 5), with minor sericite (<<1%) within calcite (Fig. 6h).

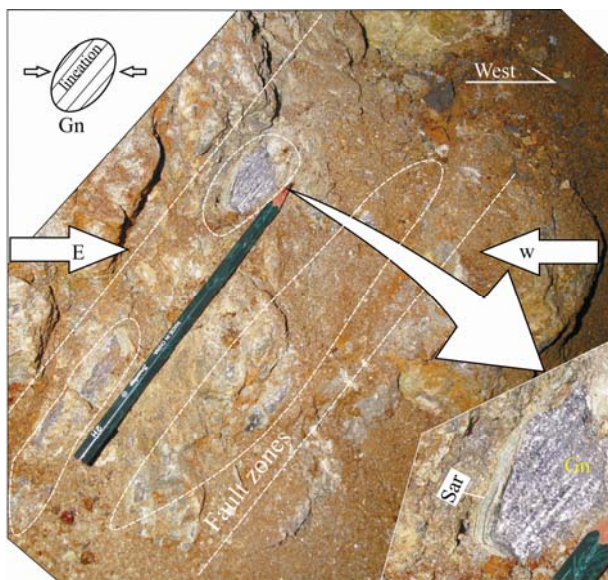


Fig. 7. Lineations in brecciated galena caused by compressional stress in the F2 fracture system.

This fault zone has undergone iron alteration causing the oxidation of the edges of brecciated galena to form anglesite. The image in the top left is a sketch of the lineations within galena formed during west to east compressional stress, and a photograph of the deformed galena is shown in the bottom right of the image. Short heavy dashed lines indicate the extent of the fracture zone and finer dashed lines indicate the extent of the breccia ore; Ang, anglesite.

#### (4) Quartz-stibnite stage B (V)

This stage is characterized by the precipitation of significant amounts of euhedral to subhedral quartz and stibnite in veins, and is divided into quartz–stibnite–sphalerite and quartz–cinnabar–gypsum substages.

**Quartz-stibnite-sphalerite substage B (V, 10):** This substage of mineralization is associated with an assemblage of quartz (40%–45%), stibnite (20%–30%), sphalerite (5%–10%), tetrahedrite (<5%), freibergite (<5%), and zinkenite (<5%). Quartz veins that formed during this substage have widths of 5–20 cm and contain euhedral to subhedral stibnite with some sphalerite (Fig. 8d1–2). A few sulfosalt minerals (e.g., freibergite, tetrahedrite, and zinkenite) were also identified by electron probe analysis of quartz–stibnite veins that crosscut previously formed sulfosalt veins (Fig. 8c).

**Quartz-cinnabar-gypsum substage B (V, 11):** This substage of mineralization is associated with a quartz (85%–90%), cinnabar (<5%), and gypsum (<5%) assemblage that is usually present as tiny veins within fissures in slate in areas distal from individual orebodies.

#### (5) Quartz stage B (VI)

This stage of mineralization is associated with the precipitation of barren comb, finger-like, cluster-like, and porous quartz deposited from ancient siliceous hot springs. This stage only has a single *quartz–sinter* substage.

**Quartz-sinter substage B (VI, 12):** This substage of mineralization is associated with the formation of siliceous quartz (30%–35%), geyselite (35%–40%), and chalcedony (20%–25%) assemblages. A thick pale yellow quartz vein that formed during this substage crosscuts all other mineralization stages within the deposit (Fig. 6i), and finger- and cluster-like euhedral quartz grows around the outside of quartz–stibnite breccias (Fig. 6g2–3). Finger- and cluster-like quartz is also associated with sinter deposits that contain adarce and geyselite (Fig. 6g1), and may be related to the remnants of ancient hot springs exposed in a valley 4 km west of Zhaxikang.

### 5 Fluid Inclusion Data

The mineral assemblages described above were used to select several stages and substages for fluid inclusions (FIs) analysis (Table 2), namely A(I, 1), B(II, 2), B(II, 4), B(III, 6), B(IV, 10), and B(V, 11) (Fig. 9). Microthermometric measurements were performed on doubly polished sections using a Linkam heating–freezing platform, with a measured temperature range from –198°C to 600°C. Accuracy of the measurements was ensured by calibrating with the triple point of CO<sub>2</sub> (–56.6°C) and the freezing point of pure H<sub>2</sub>O (0.0°C). The precision of the

temperature measurement is reproducible within 0.2°C and 2°C during freezing and heating, respectively.

Inclusions analyzed in this study include primary and pseudo-secondary inclusions, which occur as isolated clusters or trails in quartz, carbonate and sphalerite from the various ore-forming stages (Fig. 9). Main two types of inclusions, which are dominantly aqueous FIs and minor carbon dioxide-rich FIs (LC-FIs), were distinguished according to their phase composition at room temperature and during the cooling test.

Aqueous FIs (LV-type) mostly occur each stage in quartz and sphalerite. This type is lenticular, tubular, and amorphous in shape with an aqueous and a vapor phase at room temperature (Fig. 9a, b, d). Their width ranges from 3 to 8 μm, and length 4–15 μm. These FIs have low vapor content (8–15 vol.%), and liquid CO<sub>2</sub> was not observed during cooling. Fluid inclusions within the deposit are, and have an average size of 6 mm × 4 mm.

A few of carbon dioxide-rich FIs (LC-type) (Fig. 9c) are founded in stage B(II,4) sphalerite. These FIs are usually shape of short tubular and elliptical, which range from 2–4 μm in width, and 4–6 μm in length. The CO<sub>2</sub> phase accounts for 25–100 vol.% of the FIs.

The salinity of singular FIs is calculated by the empirical formula proposed by Haas (1976) and Bodnar (1993):  $\omega = 0.00 + 1.78T_{ice} - 0.0442T_{ice}^2 + 0.000557T_{ice}^3$  ( $T_{ice}$  shorts for freezing point temperature). The results are presented in Table 2.

LRM results for the vapor and liquid phases were conducted by Xie et al. (2017) and Zhu et al. (2012). The vapor and aqueous phase of LV-type FIs both in quartz and sphalerite are dominated by H<sub>2</sub>O with small amounts of gaseous CH<sub>4</sub>, N<sub>2</sub>, and C<sub>2</sub>H<sub>6</sub> (Zhu et al., 2012, Xie et al., 2017). The vapor phase in LC-type FIs is dominated by CO<sub>2</sub> and CH<sub>4</sub> with minor N<sub>2</sub>, and liquid phase is dominated by H<sub>2</sub>O.

Microthermometric results shows that the salinities and homogenization temperatures of fluid inclusions within each stage and substage of mineralization are highly variable. FIs in period A have an average homogenization temperature of 238°C and salinities of 3.74–9.18% NaCl equivalent with an average of 5.56% NaCl equivalent. In comparison, FIs in period B homogenize at 184–267°C and have highly variable salinities of 4.0–10.18% NaCl equivalent. The homogenizations temperatures increase to a maximum at substage B(III, 6) but then decrease to 187°C at B(IV, 11) that ranges from 212–233°C in stage B(II, 2), 207–228°C in stage B(II,4), 240–288°C in stage B(III, 6), 220–260°C in stage B(III, 10) to 180–190°C in , respectively. (Fig. 10). While the corresponding salinities decrease between substages B(II, 2) and B(IV, 11) that are 8.30–12.39%, 4.14–5.96% , 3.74–6.38%, 4.53–6.38%,

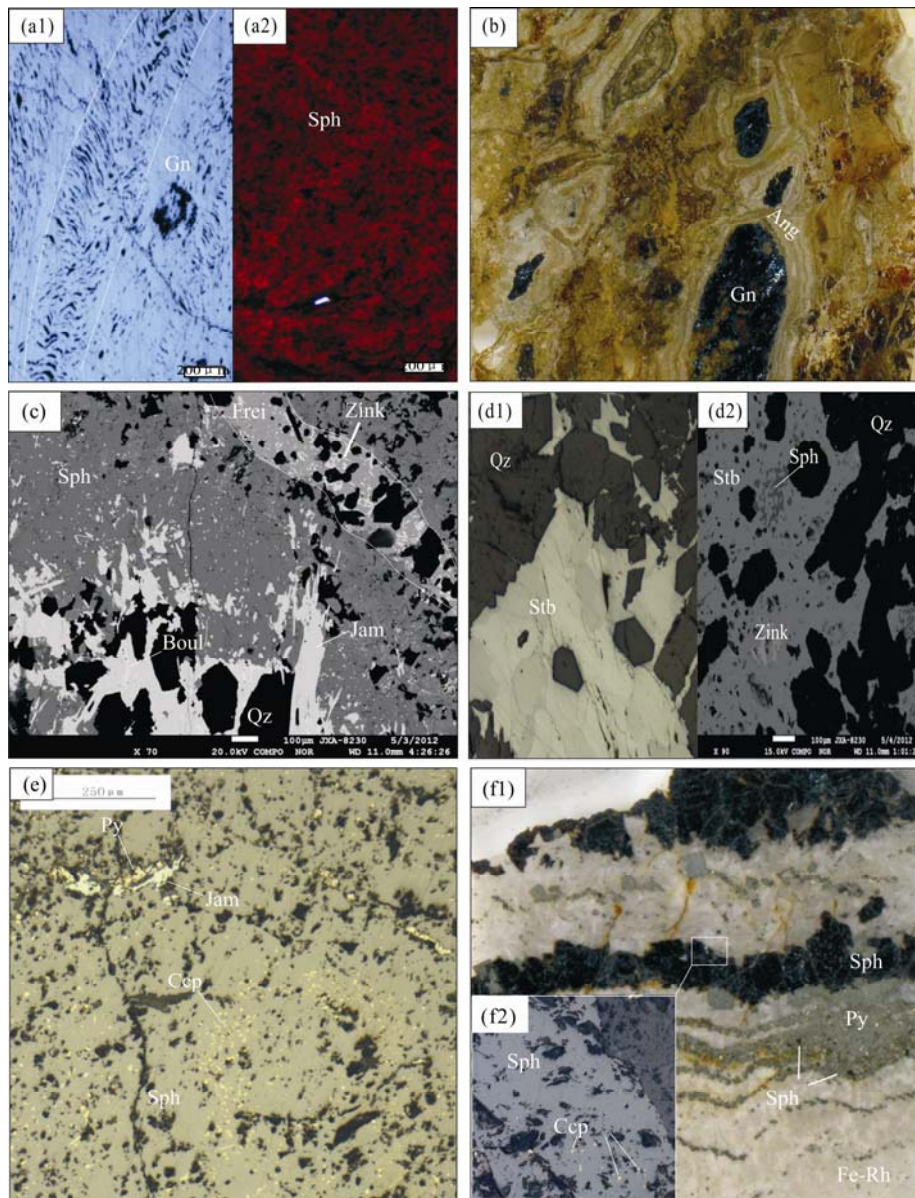


Fig. 8. Photomicrographs showing the typical microscopic mineral, structural, and textural features of mineralization within the Zhaxikang deposit.

(a), Coarse-grained galena and sphalerite formed during period A: a1, Typical triangular polishing pits within galena (reflected polarized light); a2, Dark red sphalerite (transmitted polarized light); (b), Brecciated galena with anglesite oxides (sanning figure of polished section); (c), Jamesonite and boulangerite are the two main sulfosalts in the quartz-sulfosalts-sphalerite substage of mineralization, which are crosscut by later freibergite + stibnite mineralization (reflected polarized light); (d), Quartz-stibnite stage of mineralization: d1, idiomorphic to subidiomorphic quartz + stibnite vein; d2, Quartz + stibnite vein with rare sphalerite and zinkenite (backscattered electron (BSE) image). (e) Chalcopyrite diseased sphalerite that also contains minor pyrite formed during quartz + sulfosalts + sphalerite substage of mineralization (reflected polarized light). (f) F1 = crustiform sphalerite + Fe-rhodochrosite with a Fe-rhodochrosite + pyrite + sphalerite rim (sanning figure of polished section), f2 = minor amounts of chalcopyrite in sphalerite (reflected polarized light).

**Table 2** Microthermometric and salinity data of fluid inclusions from the polymetallic Zhaxikang Pb-Zn-Ag-Sb deposit

Period	Stage, (substage)	minerals	type	n.	$T_{ice}$ (°C)			$T_h$ (°C)			salinity (wt% NaCl eqv.)		
					min	max	aver	min	max	avg.	min	max	avg.
Period A	A(I,1)	Sph	VL	20	-4.60	-2.00	-3.00	228	265	238	3.74	9.18	5.61
	B(II,2)	Sph	VL	16	-6.00	-4.20	-5.02	212	233	220	8.30	12.39	10.18
	B(II,4)	Qtz, Sph	VL/LC	8	-3.10	-2.20	-2.44	207	228	220	4.14	5.96	4.62
Period B	B(III,6)	Qtz	VL	34	-3.30	-2.00	-2.30	240	288	267	3.74	6.38	4.80
	B(III,10)	Qtz	VL	23	-3.30	-2.40	-2.81	220	260	242	4.53	6.38	5.36
	B(V,11)	Qtz	VL	6	-2.30	-2.00	-2.13	184	190	187	3.74	4.33	4.00

$T_h$ , homogenization temperature;  $T_{ice}$ , ice point temperature; Sph, sphalerite; Qtz, quartz. LV, liquid-vapor two phases inclusion; LC, liquid-carbon dioxide three phases inclusion.

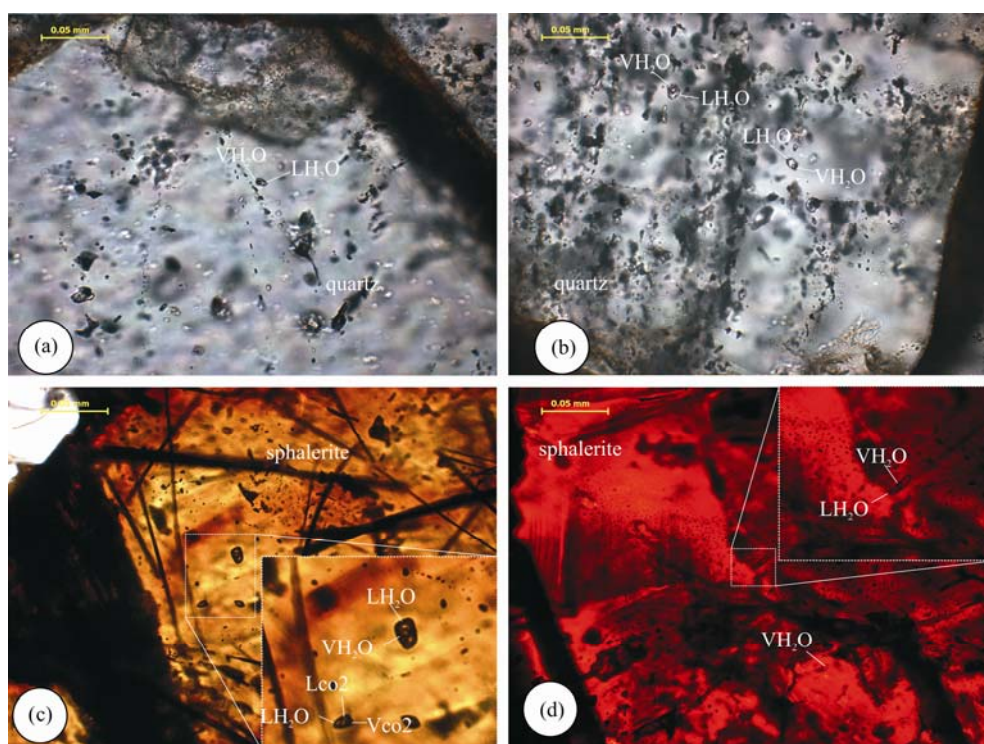


Fig. 9. Photomicrographs of fluid inclusions (FIs) in quartz and sphalerite. (a–b), LV-type FIs in stage B(III,6) and B(III,10) quartz; (c), LV- and LC-type FIs in stage B(II,4) sphalerite; (d), LV-type FIs in Stage I sphalerite. Abbreviations: VCO<sub>2</sub>, vapor CO<sub>2</sub>; LCO<sub>2</sub>, liquid CO<sub>2</sub>; LH<sub>2</sub>O, aqueous phase; VH<sub>2</sub>O, vapor phase.

and 3.74–4.33% in stage B(II, 2), B(II, 4), B(III, 6), B(III, 10) and B(III, 11), respectively.

## 6 Mineral Geochemistry

### 6.1 Analytical methods

Minerals within the Zhaxikang deposit record the replacement of individual minerals during mineralization, zoning of metals within the deposit, variations in the Fe content of sphalerite, and provide evidence of ore-forming processes recorded by S and Pb isotope variations. These data mean that this deposit is unique within the Tethyan Himalayan metallogenic belt.

Sphalerite and galena elements analysis was undertaken at the Institute of Mineral Resources, Chinese Academy of Geological Sciences, Beijing, China, by using a JXA-8230 electron microprobe with a 15 kV accelerating voltage, a 20 nA beam current, and a 5 mm beam size. Matrix corrections were undertaken using the ZAF correction program supplied by the manufacturer, and all analyses were normalized to 100%. The S and Pb isotopic compositions of stibnite, galena, sphalerite, sulfosalt minerals, and pyrite can provide evidence of the sources of sulfur and metals within these minerals, respectively. Sulfur isotope analysis was undertaken in the stable isotope laboratory of the National Research Center for Geoanalysis (NRCG), Beijing, China, and all S isotope

compositions are reported as ‰ deviation from Vienna Canon Diablo Troilite (V-CDT), with precision better than  $\pm 0.1\%$ . Single minerals for Pb isotope analysis were ground in an agate mortar to pass through a c.200 mesh and were analyzed at NRCG using a MAT-261 thermal ionization mass spectrometer. In total, the Pb isotope compositions of 21 galena, sphalerite, pyrite, sulfosalt minerals, and stibnite samples were determined during this study, 9 of which were coarse-grained galena, sphalerite, and pyrite from period A, with all others from period B. Measurements are accurate to better than 0.19‰, 0.07‰, and 0.08‰ for  $^{208}\text{Pb}/^{204}\text{Pb}$ ,  $^{207}\text{Pb}/^{204}\text{Pb}$ , and  $^{206}\text{Pb}/^{204}\text{Pb}$ , respectively (2 system error uncertainties).

### 6.2 Pb and Sb variations between galena and sulfosalts

Galena that formed during period A within orebody VI is always brecciated (Fig. 7), and records the effects of the stress field in the form of lineation (Fig. 7, right bottom). In addition, this brecciated galena is largely replaced by sulfosalt minerals (e.g., boulangerite; Fig. 11). This phenomenon is much common in the bottom of orebodies. A clear embay-shaped displacement front of boulangerite (light green) inserts into the galena (silver-white). Electron microprobe results of coarse-grained galena in period A show that the Pb elements have decreased from point 86.132 to 8.926%, and Sb increased from nearly zero to 24.764%. Minor Sb has been detected in galena, and

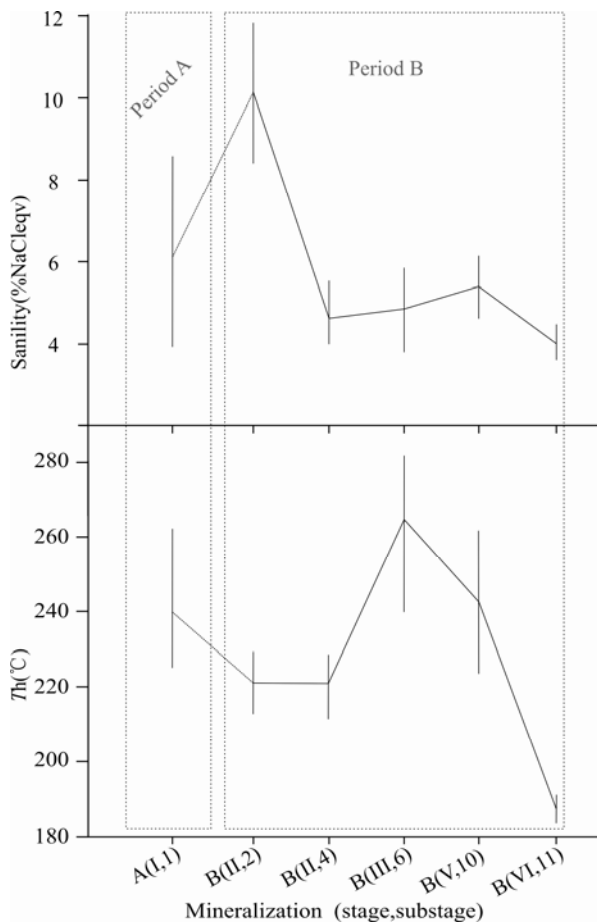


Fig. 10. Diagram showing variations in fluid inclusion salinity and homogenization temperature for the Zhaxikang.

increased small scale (0.383% –0.433%) from the centre to edge of the displacement front (Table 3).

### 6.3 Sphalerite Fe content

Brecciated coarse-grained sphalerite that formed during period A is dark black (Fig. 6 b1) and is free of chalcopyrite, whereas the later-formed sphalerite contains numerous chalcopyrite droplets. This brecciated sphalerite is also overprinted by later fluids, causing increase of Cu and loss of Fe (Fig. 12 and Fig. 13) and a systematic decrease in sphalerite Fe concentrations from core to rim (Table 4), which presents dark black to nigger-brown to light yellow.

The Fe compositions in variably textured sphalerite vary from 1.46 to 8.99 mol.% FeS (Table 5). These

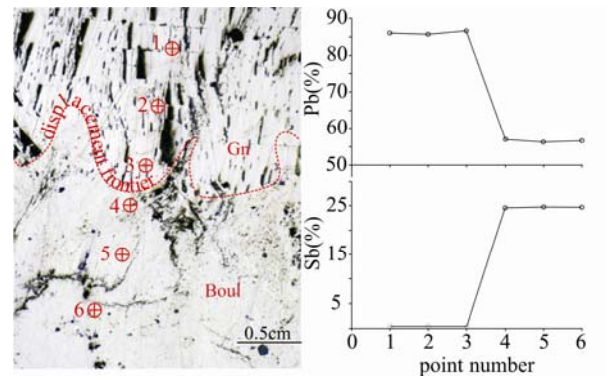


Fig. 11. Galena replaced by sulfosal minerals (boulangerite). Image on the left shows boulangerite replacing galena along a metasomatic boundary (heavy dashed line) and within the galena (reflected light), whereas the image on the right shows variations in Sb and Pb concentrations along the metasomatic boundary, with the positions of analytical points shown on the left hand image.

variations are systematic and allow the differentiation of three compositional populations corresponding to sphalerites with different textures that formed in different stages. These populations are A(I) = coarse-grained primary sphalerite that formed during period A, B(II) = coarse- to medium-grained sphalerite that formed after period A and in early stage of period B, and B(III) = fine-grained sphalerite forming within quartz–sulfosal and stibnite veins. All of these data define a linear trend in a Fe vs. Zn diagram (Fig. 12), where primary sphalerite contains the maximum amounts of Fe (8.999–9.577 mol.% Fe), sphalerite that formed during the first stage of period

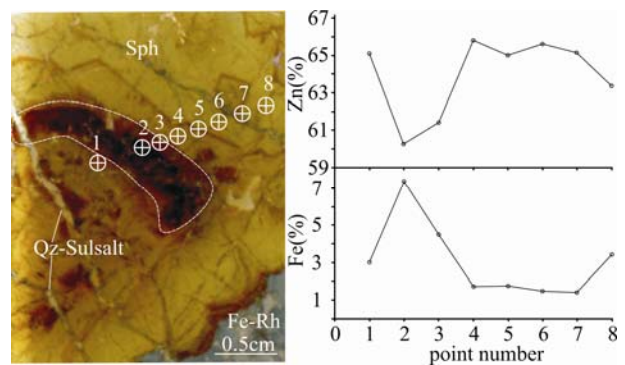


Fig. 12. Faded texture in post-overprinting sphalerite. Sphalerite formed during period A with a faded texture visible in a photomicrograph (transmitted polarized light) and with electron probe data indicating variations in Fe concentrations from the center of the sphalerite to the edge.

Table 3 Results of electron probe analysis of sulfosal mineral (boulangerite) replacing coarse-grained galena

No.	Se	S	Pb	Te	Fe	Cu	Zn	Ga	Ni	Sb	Total
1	0.029	13.793	86.132	0.003	0	0.004	0.020	0.195	0.016	0.383	100.575
2	0	13.701	85.733	0	0.033	0	0	0.304	0.013	0.432	100.216
3	0	13.622	86.652	0	0.034	0.040	0	0.390	0	0.433	101.171
4	0	19.219	56.939	0	0.044	0.009	0	0.027	0	24.608	100.846
5	0	19.181	56.331	0	0.019	0	0	0.214	0	24.796	100.541
6	0	18.926	56.700	0	0	0	0	0.061	0.009	24.764	100.460

**Table 4 Results of electron probe analysis of remobilized coarse-grained sphalerite**

No.	Se	As	S	Pb	Bi	Fe	Cu	Zn	Ni	Sb	Co	Total
1	0	0	32.249	0.242	0.020	3.002	0.004	65.046	0	0.008	0.017	100.588
2	0	0	32.188	0.097	0.053	7.345	0	60.243	0.01	0	0.028	99.964
3	0.055	0	34.057	0	0.007	4.483	0	61.398	0	0.007	0.012	100.019
4	0	0	32.167	0	0	1.712	0	65.752	0.011	0	0.001	99.643
5	0	0	33.792	0.008	0	1.748	0	64.988	0.003	0	0.005	100.569
6	0.023	0	31.952	0	0.143	1.460	0	65.610	0	0	0	32.118
7	0	0	33.582	0	0	1.411	0	65.121	0.003	0	0.004	100.181
8	0.001	0.015	34.051	0	0	3.407	0	63.348	0	0	0.002	100.900

**Table 5 Variations in the Fe–Zn–S composition of sphalerite formed during differing periods and stages of mineralization**

Period (stage)	Se	As	S	Pb	Bi	Fe	Cu	Zn	Ni	Sb	Co	Ag	Total
A(I)	0.007	0.006	32.378	0.286	0.000	8.999	0	57.324	0	0	0.011	0	99.011
	0	0	32.463	0.138	0.000	9.577	0	56.796	0	0	0.002	0.007	98.983
B(II)	0	0	32.689	0.255	0.046	9.109	0	58.030	0	0.004	0.006	0	100.143
	0	0	32.481	0.034	0.090	7.125	0.014	59.743	0	0	0.009	0	99.496
	0	0	32.188	0.097	0.053	7.345	0	60.243	0.010	0	0.028	0.005	99.969
	0	0	32.016	0.173	0.000	7.991	0.011	58.379	0	0	0.004	0	98.574
	0	0.045	32.387	0.075	0.000	7.255	0.038	59.224	0	0	0.007	0	99.041
	0	0	32.408	0.212	0.007	7.246	0	59.565	0	0	0	0	99.438
	0	0.014	32.435	0.238	0.107	7.768	0	58.317	0	0	0.017	0	98.896
	0	0	32.344	0.109	0.000	7.738	0.072	57.984	0	0.023	0.001	0	98.271
B(III)	0	0	33.940	0.000	0.000	4.499	0	61.436	0.093	0.007	0.021	0.014	100.010
	0.005	0	33.880	0.000	0.023	5.438	0	61.116	0.050	0.002	0.004	0	100.518
	0.008	0	33.677	0.000	0.000	4.407	0	61.765	0	0	0	0.013	99.870
	0.035	0	33.767	0.000	0.000	4.170	0	61.740	0.052	0.016	0.021	0.003	99.804
	0	0	34.121	0.000	0.000	4.305	0	61.303	0.030	0.001	0	0	99.760
	0	0	33.785	0.004	0.003	3.712	0	62.440	0.084	0	0.008	0.009	100.045
	0	0	32.125	0.160	0.044	2.534	0	65.505	0	0	0.002	0	100.370
	0.001	0	33.720	0.060	0.007	3.969	0.003	62.025	0.079	0	0	0.017	99.881
	0	0	32.249	0.242	0.020	3.002	0.004	65.046	0	0.008	0.017	0	100.588
	0	0	32.167	0.000	0.000	1.712	0	65.752	0.011	0	0.001	0	99.643
0.023	0	31.952	0.000	0.143	1.460	0	65.610	0	0	0	0	99.188	

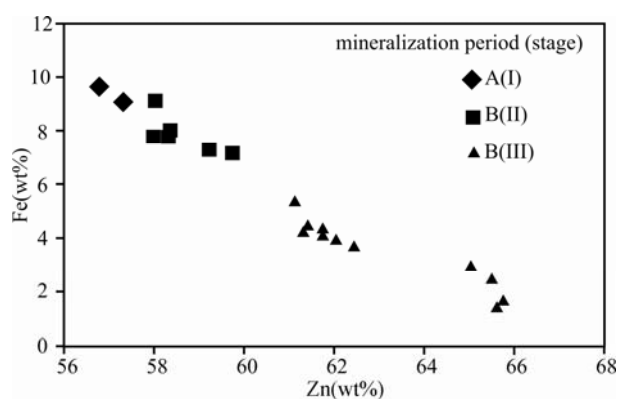


Fig. 13. Composition of sphalerite that formed during differing period (stage) of the Zhaxikang deposit.

These differing periods and stages record a regular decrease in sphalerite Fe content over time.

B has lower Fe concentrations (7.125–9.109 mol.% Fe), and B(III) sphalerite has significantly lower Fe concentrations that define two groups with Fe concentrations of 5.438–3.969 and 3.002–1.460 mol.%.

#### 6.4 Variations of elements composition

The economic metals in Zhaxikang contain Pb, Zn, Sb and Ag, which geochemical data of drill 701 and ore-veins 703 in 4710 level used in this study were according to the detailed exploration report by Huayu Ltd. Co. (2009).

The economic metals within the deposit (i.e., Pb, Zn,

Ag, and Sb) vary regularly both laterally and vertically, This is exemplified by orebody V (Fig. 2b), which is divided into Pb + Zn, Pb + Zn + Sb, Zn + Sb, and Sb zones from bottom to top side. These four elements are approach to a normal distribution in drillhole 701 (Fig. 14). The most Pb, Zn, Ag, and Sb concentrated in sea level 4667–4687 meters. In this area, Pb, Sb and Ag have the same change law that are positively correlated with each other in the center of the orebody (middle of Fig. 14), while broken of the law in the peripheries of ores (edges of Fig. 14). Therefore, it can be divided into Pb-Zn coupled region in middle part and Pb-Sb decoupled in two sides. In addition, three types of Pb and Sb curves can be recognized within central orebody that concentration of Pb > Sb in the much center of the orebody and Pb < Sb at the margins of this central area (Fig. 14). The Zn concentration curve in a vertical direction is more or less similarity to the variations of Pb, Sb and Ag curves with the depth.

The lateral variations of these elements are much similar to the vertical variations described above, which shows normal distribution along CM703 in 4710 level (Fig. 15). Pb and Sb concentrations are coupled in central region, where contains a core with higher concentrations of Pb than Sb, and margins with higher Sb concentrations than Pb. In two sides, the Pb, Sb and Ag are decoupled,

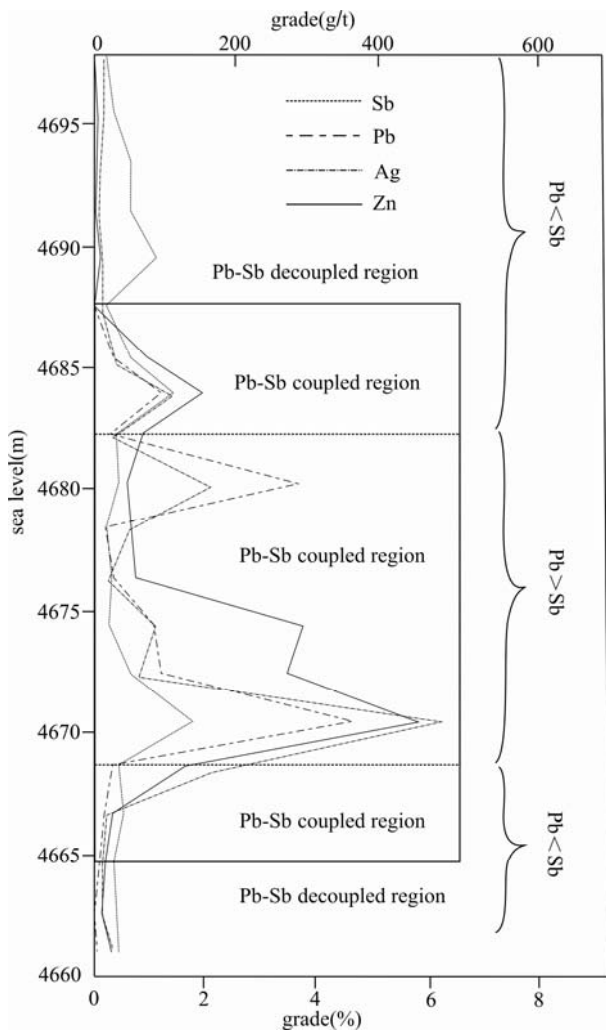


Fig. 14. Vertical variation of Pb, Zn, Ag and Sb of drill 701. Grade unit of Ag is (g/t); the others are percentage(%).

whereas an increase in Sb concentrations with distance from the center of the orebody, but Pb and Ag concentrations decrease rapidly within the decoupled area.

Zn concentration curve seems to different change law from the Pb, Ag and Sb concentration curves (Fig. 15), it more like a shape of hill while others change as shape of saw.

### 6.5 Isotopic data

We present S and Pb isotopic data here from the pure minerals containing sphalerite, galena, pyrite, stibnite and sulfosalt minerals. It is difficult to separate a mineral from an exact stage veins, for there are minerals in several different stage usually, therefore, we only could identify their forming period.

#### 6.5.1 Sulfur isotopes

The S isotope compositions of sulfide minerals from periods A and B that were determined during this study and those previously reported by Yang et al. (2009) are given in Table 6. These samples have  $\delta^{34}\text{S}_{\text{V-CDT}}$  values of 4.5‰–13.2‰, consisting of 11.2‰–13.2‰ of sphalerite, 11.2‰–12.7‰ of pyrite, 9.9‰ of galena. Period A galena, sphalerite, and pyrite yielded a narrow range of positive  $\delta^{34}\text{S}_{\text{V-CDT}}$  values (9.9‰–13.2‰) that are little higher than the range of the period B samples (7.2‰–12.1‰; Fig. 16b). In period B, sphalerite from the deposit yields the highest  $\delta^{34}\text{S}_{\text{V-CDT}}$  values of 9.1‰–12.1‰, followed by galena and sulfosalt minerals (boulangerite) with 9.4‰ and 8.7‰–11.2‰ in pyrite, while stibnite yielding the lowest  $\delta^{34}\text{S}$  values of 4.5‰–9.2‰ (Fig. 16b). However, the S

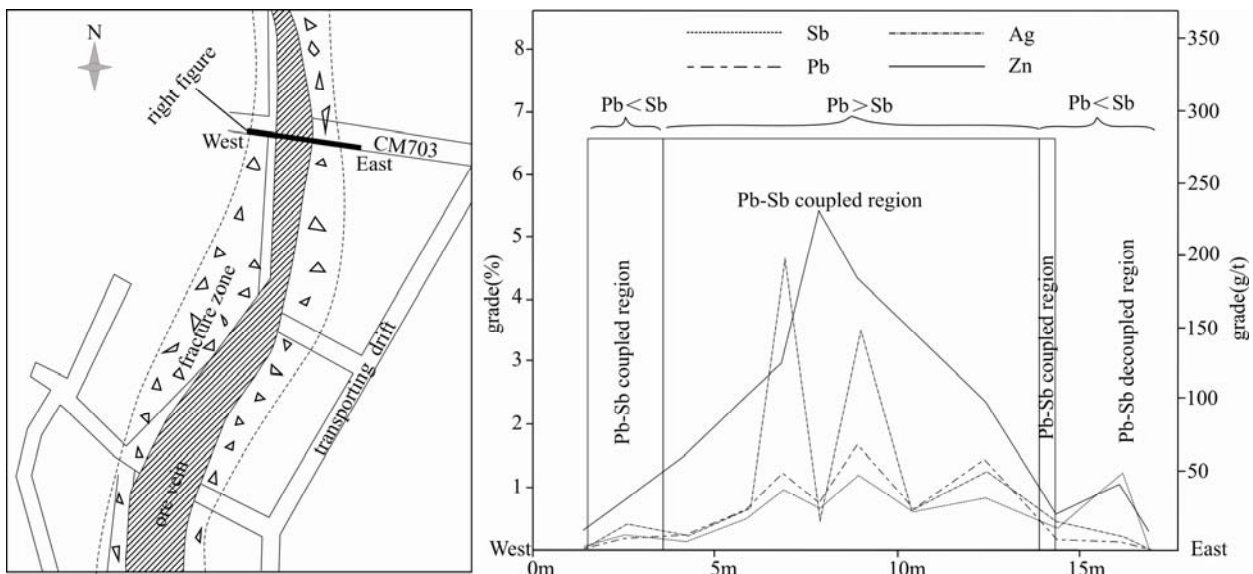


Fig. 15. Lateral contents variation of Pb, Zn, Ag and Sb.

Left image: plane graph of cross vein 703 of Zhaxikang 4710 level; Right image, elements variation from west to east side; grade unit of Ag is (g/t); the others are percentage (%).

**Table 6 Variations in  $\delta^{34}\text{S}_{\text{V-CDT}}$  compositions of sulfides formed during the two mineralization periods**

Period	Samples	Mineralization	Mineral	$\delta^{34}\text{S}_{\text{V-CDT}}(\text{‰})$	Data source
Period A	ZXK06-25	coarse sphalerite vein (early)	Sphalerite	12	Yang et al., 2009
	ZXK06-26	coarse sphalerite vein (early)	Sphalerite	11.4	Yang et al., 2009
	ZXK06-26	coarse sphalerite vein (early)	Pyrite	11.2	Yang et al., 2009
	ZXK2-3	coarse sphalerite vein (early)	Sphalerite	11.2	Yang et al., 2009
	ZXK2-3	coarse sphalerite vein (early)	Galena	9.9	Yang et al., 2009
	cb-138	stratiform-like sphalerite	Sphalerite	11.8	This study
	cb-149	coarse sphalerite with rhodochosite	Sphalerite	12.6	This study
	cb-149	coarse sphalerite with rhodochosite	pyrite	12.1	This study
	cb-138	stratiform-like sphalerite	galena	10.1	This study
	cb-146	coarse galena breccia	galena	9.9	This study
	cb-122	sphalerite with rhodochosite	Sphalerite	13.2	This study
	cb-138	stratiform-like sphalerite	pyrite	11.6	This study
	cb-139	stratiform-like sphalerite	pyrite	12.7	This study
	cb-134	sphalerite with galena vein	Sphalerite	12.3	This study
Period B	ZXK04-2	quartz–stibnite vein	Stibnite	4.5	Yang et al., 2009
	ZXK-3	quartz–stibnite–sphalerite vein	Stibnite	7.1	Yang et al., 2009
	ZXK-5	quartz–stibnite–sphalerite vein	Sphalerite	9.1	Yang et al., 2009
	ZXK-6	quartz–arsenopyrite vein with sphalerite breccia	Sphalerite	11.1	Yang et al., 2009
	ZXK06-15	quartz–pyrite vein	Pyrite	8.9	Yang et al., 2009
	ZXK06-23	quartz–pyrite vein	Pyrite	8.7	Yang et al., 2009
	ZXK06-21	pyrite vein	Pyrite	10.6	Yang et al., 2009
	ZXK1-1	quartz–stibnite–sphalerite vein	Sphalerite	10.2	Yang et al., 2009
	ZXK1-3	quartz–stibnite–sphalerite vein	Sphalerite	10.6	Yang et al., 2009
	ZXK1-4	quartz–stibnite–sphalerite vein	Sphalerite	10.4	Yang et al., 2009
	ZXK1-5	quartz–stibnite–sphalerite vein	Sphalerite	10.4	Yang et al., 2009
	ZXK1-9	quartz–stibnite–sphalerite vein	Sphalerite	9.7	Yang et al., 2009
	cb-126	quartz–sphalerite vein	Sphalerite	11.8	This study
	cb-132	massive galena with sphalerite	Sphalerite	12.1	This study
	cb-139	stratiform-like sphalerite	Sphalerite	10.6	This study
	cb-140	stockwork sphalerite and stibnite vein	Sphalerite	11.5	This study
	cb-151	fine sphalerite vein	Sphalerite	10.9	This study
	cb-121	quartz–Sulfosalt	Sulfosalt	9.4	This study
	cb-132	quartz–sphalerite	Stibnite	8.6	This study
	cb-139	quartz–sphalerite	Stibnite	7.2	This study
	cb-140	quartz–sphalerite	Stibnite	8.1	This study
	cb-151	quartz–sphalerite	Stibnite	9.2	This study
	cb-132	massive galena with sphalerite	Pyrite	11.2	This study
	cb-132	massive galena with sphalerite	Galena	9.4	This study

isotope compositions of samples from the Zhaxikang deposit differ from those of other Sb-Au deposits in this area, which have values between ~5‰ and 0‰ (Fig. 16a). The S isotope composition of south Tibet sedimentary rocks is relatively higher than the period B that is around 10‰ (Fig. 16a).

### 6.5.2 Lead isotopes

The Pb isotopic data for samples from the Zhaxikang deposit are given in Table 7. All of these samples have relatively uniform but high radiogenic compositions, with  $^{206}\text{Pb}/^{204}\text{Pb}$ ,  $^{207}\text{Pb}/^{204}\text{Pb}$ , and  $^{208}\text{Pb}/^{204}\text{Pb}$  values of 19.3391–19.7848, 15.7816–15.8473, and 39.8368–40.2711, respectively. Sulfide minerals that formed during period A contain slightly less radiogenic Pb, yielding  $^{206}\text{Pb}/^{204}\text{Pb}$  ratios of 19.3391–19.7332 corresponding to 19.6644–19.7848, and  $^{207}\text{Pb}/^{204}\text{Pb}$  15.7816–15.8373 values compared to values of 15.8295–15.8473 for period B samples (Table 7). The samples analyzed during this study have relatively high  $\mu$  ( $^{238}\text{U}/^{204}\text{Pb}$ ) values (9.54–9.82) and

$\varphi$  ( $^{235}\text{U}/^{204}\text{Pb}$ ) values (0.5247–0.54065), with a narrow range of  $\omega$  ( $^{242}\text{Th}/^{204}\text{Pb}$ ) values (38.62–38.98), and low Th/U values (3.81–4.32; Table 7);  $\mu$ ,  $\varphi$  and  $\omega$  values and Th/U ratios were calculated using Isoplot 2.0 (Ludwig, 2003). Sulfosalt minerals and stibnite contained similar amounts of and highest radiogenic Pb isotope in period B, whose  $^{206}\text{Pb}/^{204}\text{Pb}$ ,  $^{207}\text{Pb}/^{204}\text{Pb}$ , and  $^{208}\text{Pb}/^{204}\text{Pb}$  values are 19.7597–19.7857, 15.8421–15.8473, and 40.2365–40.2711, respectively. Sphalerite in period A has lowest radiogenic Pb isotope that  $^{206}\text{Pb}/^{204}\text{Pb}$ ,  $^{207}\text{Pb}/^{204}\text{Pb}$ , and  $^{208}\text{Pb}/^{204}\text{Pb}$  values are 19.3391–19.694, 15.7816–15.8306, and 39.209–40.2090, respectively. Further more, the amount of radiogenic Pb within galena varies significantly between periods A and B (Fig. 17) are much similar and vary narrowly from 19.6644–19.7135, 15.8299–15.8359 and 40.1594–40.2009 for  $^{206}\text{Pb}/^{204}\text{Pb}$ ,  $^{207}\text{Pb}/^{204}\text{Pb}$ , and  $^{208}\text{Pb}/^{204}\text{Pb}$  values. All Pb isotopic data define a clear linear trend in both  $^{206}\text{Pb}/^{204}\text{Pb}$ – $^{207}\text{Pb}/^{204}\text{Pb}$  and  $^{206}\text{Pb}/^{204}\text{Pb}$ – $^{208}\text{Pb}/^{204}\text{Pb}$  diagrams that plots away from the crustal growth curve (C curve in Fig. 17) of Zartman and Doe (1981).

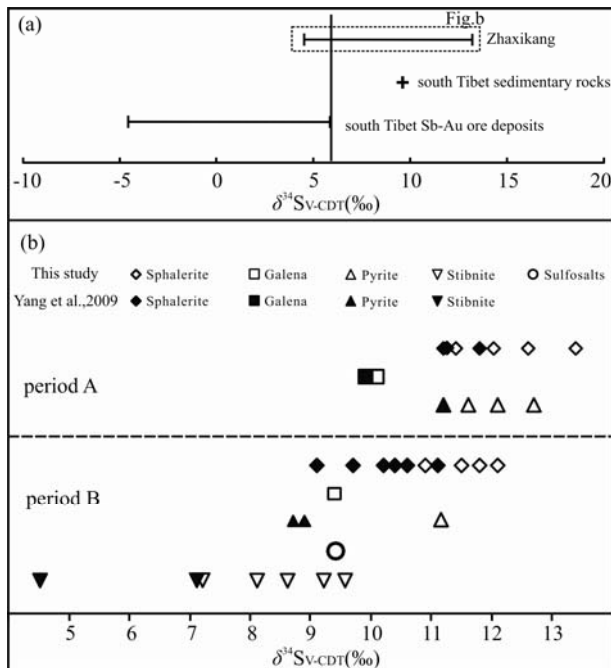


Fig. 16. Variations in S isotope compositions in samples from the polymetallic Zhaxikang Pb-Zn-Ag-Sb deposit, indicating that earlier stage mineralization is associated with much higher  $\delta^{34}\text{S}$  values.

(a), Composition between the Zhaxikang deposit, other antimony-gold deposits in southern Tibet, and sediments within south Tibet sedimentary rocks; (b), Variations in S isotope composition of different minerals formed during periods A and B; Open symbols indicate data obtained during this study; Solid symbols indicate data from Yang et al., (2009).

## 7 Discussion

All of the characteristics of the Zhaxikang deposit,

including the record of complex mineralizing processes, ore textures and structures, regular variations in sphalerite Fe concentrations, the zoning of economic elements and fluid inclusion compositions, and the S and Pb isotopic compositions of samples from the deposit, suggest that the formation of this deposit involved different processes than those other Au, Au(Sb), Pb-Zn deposits within the Himalaya. This deposit most likely formed during overprinting and remobilization associated with the Indo-Asia continental collisional setting, similar to polymetallic deposits of the Rheinisches Schiefergebirge district of Germany (Wagner and Schneider, 2002).

### 7.1 Processes involved in the formation of the Zhaxikang deposit

A possible Pb-Zn metallogenic belt in the southern Tethyan Himalaya has been suggested by previous research (Rui Zongyao et al., 2004; Qi Xuexiang et al., 2008), and has the potential to host significant yet undiscovered mineralization (Zhang Jianfang, 2012). The majority of Sb, Au, and Sb-Au deposits discovered to date are associated with metamorphic core complexes of the northern Tethyan Himalaya and define an antimony-gold metallogenic belt (Nie Fengjun et al., 2005; Yang et al., 2009), with several Sb-Pb-Zn deposits located between these two belts. This type of spatial relationship provides evidence of the tectonic conditions needed for the overprinting and remobilization of Sb-bearing mineralization and Pb-Zn sulfides to form Sb-Pb-Zn-type deposits.

Table 7 Pb isotopic compositions of samples from the Zhaxikang deposit

period	sample	mineral	$^{208}\text{Pb}/^{204}\text{Pb}$	$^{207}\text{Pb}/^{204}\text{Pb}$	$^{206}\text{Pb}/^{204}\text{Pb}$	$\phi$	$\mu$	$\omega$	Th/U
Period A	cb-119	sphalerite	39.8368	15.7816	19.3391	0.5247	9.54	42.59	4.32
	cb-122	sphalerite	40.1963	15.8253	19.6721	0.5247	9.54	42.59	4.32
	cb-138	sphalerite	40.209	15.8306	19.694	0.5247	9.54	42.65	4.33
	cb-149	sphalerite	40.1353	15.8231	19.6557	0.5395	9.81	38.42	3.79
	cb-119	pyrite	40.1417	15.8263	19.6505	0.5395	9.81	38.76	3.82
	cb-138	pyrite	40.1976	15.8296	19.6890	0.5390	9.80	38.72	3.82
	cb-149	pyrite	40.2119	15.8373	19.7332	0.5401	9.82	38.62	3.81
	cb-119	galena	40.1709	15.83	19.6781	0.5400	9.81	38.76	3.83
	cb-146	galena	40.2009	15.8359	19.7135	0.5395	9.81	38.67	3.81
	Period B	cb-126	sphalerite	40.2113	15.8316	19.7088	0.5247	9.54	42.62
cb-132		sphalerite	40.1636	15.8295	19.6698	0.5247	9.54	42.45	4.31
cb-139		sphalerite	40.2445	15.8395	19.7716	0.5274	9.59	43.01	4.34
cb-140		sphalerite	40.2557	15.8431	19.7798	0.539	9.80	38.98	3.85
cb-151		sphalerite	40.2389	15.8436	19.7630	0.539	9.80	38.97	3.85
cb-132		galena	40.1594	15.8299	19.6644	0.5395	9.81	38.71	3.82
cb-121		sulfosalt	40.2711	15.8465	19.7848	0.5406	9.83	38.66	3.81
cb-139		stibnite	40.2703	15.8473	19.7841	0.5406	9.83	38.67	3.81
cb-140		stibnite	40.2689	15.846	19.7857	0.5406	9.83	38.65	3.81
cb-151		stibnite	40.2365	15.8421	19.7597	0.5401	9.82	38.62	3.81
cb-132		pyrite	40.1756	15.8337	19.6740	0.5395	9.81	38.76	3.82
cb-139		pyrite	40.1972	15.8334	19.7122	0.5395	9.81	38.64	3.81

Footnote:  $\phi = \frac{^{235}\text{U}/^{204}\text{Pb}}{^{238}\text{U}/^{204}\text{Pb}}$ ;  $\mu = \frac{^{238}\text{U}/^{204}\text{Pb}}{^{235}\text{U}/^{204}\text{Pb}}$ ; subscript of  $d(t)$  represents testing value at time of ore-forming, meanwhile  $m(t)$  represents the mantle value at the same time which thought to be ~20 Ma; All values are calculated by isoplot program (Ludwig, 2003). Thorium and Uranium in sulfide are (14–81) ppb and (4–37) ppb, respectively. in diabase are (2000–3630) ppb and (530–910) ppb, respectively., in carbonaceous slate are (11400–16500) ppb and (1390–1700) ppb, respectively (c. f. Zhang Jianfang et al., 2010).

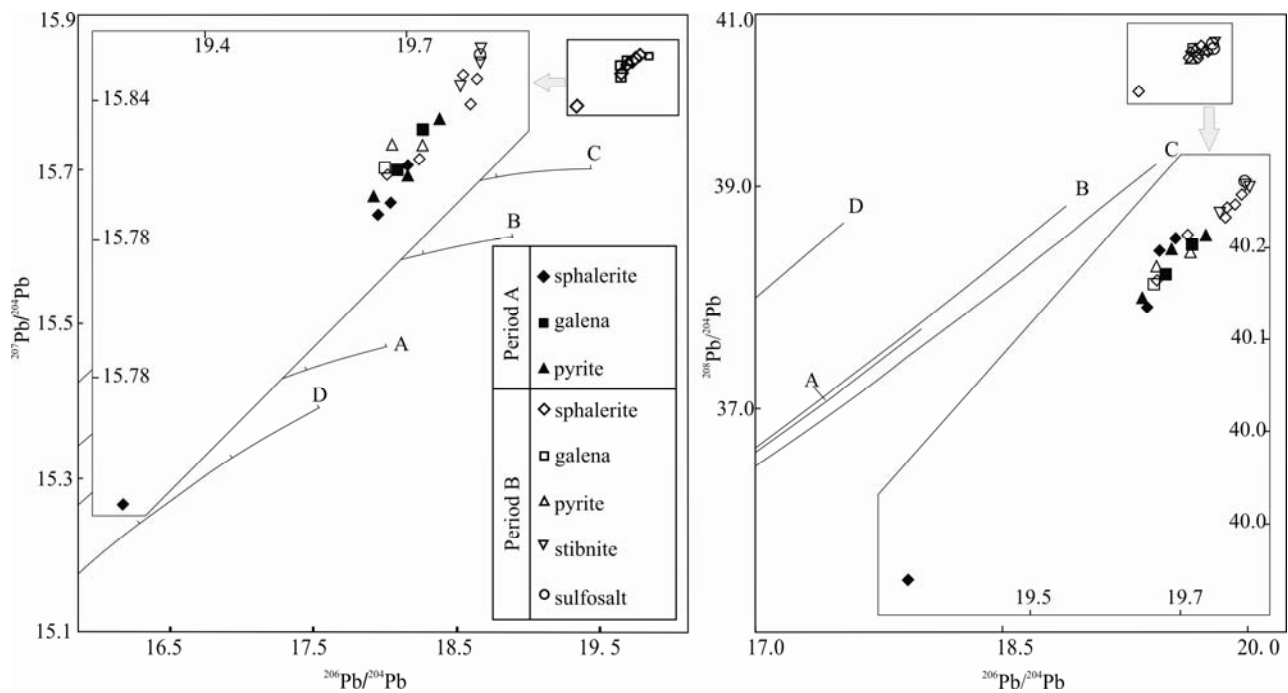


Fig. 17. Variations in Pb isotope compositions for samples from the study area, indicating that these compositions plot significantly away from the earth growth curves proposed by Zartman and Doe (1981; where A, B, C, and D indicate mantle, orogen, upper crustal, and lower crustal sources, respectively).

The Pb isotope compositions of samples from the study area define a clear trend in both  $^{206}\text{Pb}/^{204}\text{Pb}$ - $^{207}\text{Pb}/^{204}\text{Pb}$  and  $^{206}\text{Pb}/^{204}\text{Pb}$ - $^{208}\text{Pb}/^{204}\text{Pb}$  diagrams, although minerals that formed during period B contain more radiogenic Pb than those that formed during period A. In addition, sulfosalt mineral and stibnite contain more radiogenic Pb than pyrite and galena, although the amount of radiogenic Pb contained by sphalerite varies significantly compared with the other four minerals.

The lineation structures within brecciated galena that formed during the Pb-Zn period of mineralization are indicative of tectonic stress, and such structures are not evident in the Sb-bearing period of mineralization, where the majority of mineralization is present as open-space fills. This phenomenon indicates that a possible regional extruding tectonic event has appeared between period A and B, in other words, there might be a time gap within these two mineralization periods. Characteristics of Fe and Zn isotopes have indicated two pulses of mineralization in this deposit (Wang et al., 2017). Moreover, Radiogenic isotopic dating has revealed that brecciated coarsed-grained Pb-Zn ores formed at about 20.48 Ma by pyrite Re-Os dating (Zhou Qing unpublished data), which are same with 21.3 Ma Ar-Ar age of the Keyue Pb-Zn deposit (Lin Bin et al., 2014) that about 4km east to the Zhaxikang. Sericite from quartz-stibnite veins yielded a 12 Ma Ar-Ar age (Liang Wei et al., 2015) indicates that activity of Sb-bearing fluid was 8 Ma later than the Pb-Zn mineralization. The Zhaxikang has centralized two mineralization epochs in a place that could lead it to significant larger ore reserves than the other deposits within Himalaya orogeny.

Electron microprobe data of Zinc and galena of earlier period data indicate visualized genetic relationship between period A and B. The presence of Sb-Pb and/or Ag

sulfosalt minerals, and replacement of earlier galena by boulangerite during the Sb-bearing period of mineralization indicate that the Sb-bearing fluid influenced pre-existing Pb-Zn sulfides and sulfide breccias. The deformation of the Pb-Zn sulfides and subsequent replacement earlier galena and sphalerite by Sb-bearing fluids imply some form of physical and chemical remobilization and transformation, respectively (Zheng et al., 2012), indicating that significant overprinting and remobilization occurred during the formation of the Zhaxikang deposit.

The regular variations in sphalerite Fe concentrations within the deposit may be the result of corrosion, dissolution, remobilization, and reprecipitation during hydrothermal overprinting by later regionally derived Sb-bearing fluids (Wagner and Cook, 1998). The Fe compositional zoning in A(I) sphalerite breccias (Fig. 12) is also indicative of the diffusion of Fe and Zn during post-depositional re-equilibration associated with overprinting of Sb-bearing fluids (Mizuta, 1988). In addition, significant Fe depletions may be related to the presence of numerous chalcopyrite inclusions (Moles, 1983; Mizuta and Scott, 1997), which is consistent with the abundance of chalcopyrite droplets during the Sb-dominated periods of mineralization. Later regional Sb-bearing fluids may also have driven this overprinting (Bente and Doering,

1995), although this may have been prevented by a significant chemical potential gradient between zones of compositional difference in and between individual sphalerites (Bente and Doering, 1995).

The hydrothermal overprinting within the deposit relates to disequilibrium between the newly introduced fluid and the primary sphalerite within existing vein assemblages, which would have caused an equilibration of sphalerite compositions by diffusion (Wagner and Cook, 1998). The “de-iron” process of earlier could be the phenomenon of diffusion. Therefore, the early-formed Pb–Zn sulfides may have acted as an effective chemical barrier for the later Sb-bearing fluids (Zheng et al., 2012), which was more beneficial for fluid precipitation during chemical reactions with the existing Pb–Zn or bodies.

The rapidly induced and extensive variations in the Fe content of sphalerite in the deposit cannot just be the result of chemical overprinting but also must have involved physical remobilization. The Fe content of sphalerite is dependent on a series of physical and chemical variables ( $T$ ,  $p$ ,  $E_h$ ,  $pH$ , and  $f_s$ ), although temperature and sulfur fugacity are the most important of these factors. These crucial factors also both positively correlate with Fe concentrations (Hutchison and Scott, 1981; Zheng et al., 2012). The color of sphalerite depends on Fe composition, which is positive to the forming temperatures in fixed sulfur fugacity. 10–20%, 3–10% and 1–3% of Fe composition in sphalerites represent hypothermal, mesothermal and epithermal ores, respectively, while their colors correspond to deep dark, brown and yellow (Yin Xiuzhang and Hu Aizhen, 2004).

The emergence of highest Fe composition of sphalerite in A(I) shows relative high temperature ( $\sim 238^\circ\text{C}$ , FIs data) in earlier sulfides. In period B, temperature is relatively low till forming of sulfosalt minerals, and the corresponding color of sphalerites are slightly shallow to light black (Fig. 8f). There could be a pulse of heat inputting during formation of sulfosalt minerals, whose FIs temperature are about  $267^\circ\text{C}$  with nigger-brown sphalerites (Fig. 9c). The high forming temperature could not bring more Fe composition, but emergence of many copper droplets in this stage (Fig. 8e), which demonstrate Cu replace Fe in the ore-forming fluids, and the sulfur fugacity is changeable because of forming mounts of quartz.

The high-temperature sulfosalt mineralization suggests that heat was continually supplied to this area during Sb-bearing mineralization. The close spatial relationship between quartz–antimony and/or gold veins and Pb–Zn–Ag–Sb vein systems means that the relatively rapid cooling of ore-forming fluids should have significantly affected the diffusion kinetics of sphalerite, leading to the observed

incomplete equilibration of Fe in sphalerite during the later period of mineralization. This indicates that chemical energy,  $P$ , and  $T$  conditions were all important controls on the variations of sphalerite Fe concentrations during the Sb-bearing fluid-related overprinting and remobilization events in the study area.

The zonation of individual orebodies from deep Pb + Zn zones through Pb + Zn + Ag + Sb and Zn + Sb zones to uppermost Sb zones at first glance may seem to relate to temperature variations. However, this cannot explain the change between coupled and decoupled relationships between Pb, Ag, and Sb, or the distinct variations in Zn concentrations (Figs. 14, 15). Galena and sulfosalt minerals host Pb–Sb  $\pm$  Ag, whereas Zn is only present as ZnS, potentially explaining some of the variations between Zn and these other three metals. The coupled area of Pb, Ag, and Sb mineralization is dominated by sulfosalt minerals, suggesting that the center of the orebody has undergone significant remobilization and overprinting (Wagner and Boyce, 2001). Pb and Zn can be remobilized from pre-existing Pb–Zn sulfides, as is evidenced by the linear trend in Pb isotopic compositions for these sulfides. The mixing of the overprinting Sb-bearing fluid and fluids containing Pb and Zn from remobilized early-formed sulfides to form a new mineralizing fluid is one possible process that can lead to the zonation of metals within the Zhaxikang deposit (Liang Wei et al., 2013). Decreasing the temperature of a Zn + Pb + Sb  $\pm$  Ag-bearing fluid will cause precipitation of low-Fe sphalerite and sulfosalt minerals in addition to chalcopyrite and arsenopyrite. The main cause of both vertical and lateral variations in Sb and Pb concentrations within the coupled area may depend on the extent of overprinting and remobilization of pre-existing Pb–Zn sulfides by Sb-bearing fluids. The presence of relict pre-existing brecciated orebodies that have undergone replacement by sulfosalt minerals suggests that these orebodies were incompletely remobilized during metasomatism. This type of process usually initiates at the edge of an area of mineralization before proceeding to the center, generating a core with higher Pb concentrations than Sb, whereas the opposite is true at the more intensely replaced edges. The decoupled areas of mineralization that have increasing concentrations of Sb and rapidly decreasing concentrations of Pb and Ag indicate that more Pb was mobilized with Sb and/or Ag, and was removed from these areas, whereas Sb may have been supplied by regional Sb-bearing fluids that eventually precipitated Sb as stibnite without Pb during the quartz–stibnite stage of mineralization.

The evolution of the fluids associated with the deposit reflects the diversity of heat and rock/water ratios between the differing stages of mineralization. The highest-

temperature fluid is associated with the quartz–sulfosalt–arsenopyrite stage of mineralization (Fig. 8), suggesting that the most intense overprinting and remobilization was associated with an injection of heat into the Zhaxikang area. One possible heat source is the emplacement of leucogranite magmas during the Miocene that formed during anatexis of the lower crust of southern Tibet (Zeng Lingsen et al., 2009; Zhang et al., 2012), which are contemporary with the Sb-bearing mineralization. The regional Sb-quartz veins in Zhaxikang area are regarded as close relationship with the Conadong leucogranite that ~10 km south to the Zhaxikang by studying of fluid inclusion (Xie et al., 2017). Igneous-derived heat may also have driven the formation of Sb–Au mineralization in southern Tibet (Yang et al., 2009). In addition, the H–O isotopic compositions of samples from the Zhaxikang deposit indicate that the Sb-bearing fluids were geothermal waters that infiltrated and interacted with meteoric water in a system driven by magmatic heat (Yang et al., 2009; Zhang Jianfang, 2010). The remobilization of ores, infiltration of meteoric water, and the precipitation of minerals from ore-forming fluids can cause variations in water/rock ratios that are reflected by changes in fluid salinity. A continuous supply of heat also increases the circulation of geothermal fluids that interacted with the remobilized and overprinted fluids, causing an increase in water/rock ratio that is reflected by decreasing fluid inclusion salinities during the formation of Sb-bearing mineralization.

Rye and Ohmoto (1972) emphasized that total sulfur in solution ( $\delta^{34}\text{S}_{\Sigma\text{S}}$ ) values could only be used to discuss the origin of sulfur in ore deposits; these values relate to the physical and chemical conditions of hydrothermal fluids (T, pH, and  $f_{\text{O}_2}$ ) as well as the isotopic composition of sulfur within the system. These parameters are generally difficult to determine during  $\delta^{34}\text{S}_{\Sigma\text{S}}$  calculations, although sulfide minerals precipitate from solutions with  $\delta^{34}\text{S}_i$  values similar to  $\delta^{34}\text{S}_{\Sigma\text{S}}$  values in  $\text{H}_2\text{S}$ -dominated systems under low- $f_{\text{O}_2}$  conditions and involving low-pH fluids (Ohmoto, 1972). The Zhaxikang deposit formed under exactly these conditions, was sulfate-free during both periods of mineralization, and is located in an area containing both ancient and modern hot springs that contain significant amounts of  $\text{H}_2\text{S}$  gas (Li Guangming et al., 2005). This indicates that the Zhaxikang deposit has  $\delta^{34}\text{S}_{\Sigma\text{S}}$  values of 4‰–13‰ (Fig. 16a), reflecting values of 10‰–13‰ and 4‰–11‰ for periods A and B, respectively (Fig. 16b). Another factor should be considered that fractionation of different sulfides could lead to the variation of sulfur isotope. In established isotopic equilibrium area, sulfur isotope of pyrite, sphalerite and galena should be  $\delta^{34}\text{S}_{\text{pyrite}} > \delta^{34}\text{S}_{\text{sphalerite}} > \delta^{34}\text{S}_{\text{galena}}$  (Ohmoto,

1972), while in period A, the relationship of sulfur isotopes are  $\delta^{34}\text{S}_{\text{sphalerite}} > \delta^{34}\text{S}_{\text{pyrite}} > \delta^{34}\text{S}_{\text{galena}}$ , which are same with that of Period B, moreover,  $\delta^{34}\text{S}_{\text{sphalerite}}$ ,  $\delta^{34}\text{S}_{\text{pyrite}}$  and  $\delta^{34}\text{S}_{\text{galena}}$ , in period A are the tendency higher than each of them in period B. Therefore, the isotopic variation of sulfur reflects the real characteristics of S sources.

The relatively high  $\delta^{34}\text{S}$  of period A sulfides are similar to pyrite in Cretaceous sediments (Li Jin'gao et al., 2002) suggesting earlier sulfur can be the sedimentary source. The Sb–Au mineralization in the study area contains magmatic sulfur with  $\delta^{34}\text{S}$  values around zero (Yang et al., 2009), suggesting that the Sb-bearing fluid formed about ~12 Ma has similar S isotope values. In period B, stibnite forms in later stage with lower S isotopic compositions than sphalerite and galena, which demonstrate decreasing of  $\delta^{34}\text{S}$  values. The gradually decreasing in  $\delta^{34}\text{S}$  values of the Sb-bearing mineralization within the deposit suggest that these ores contain sulfur derived from both the Pb–Zn sulfides and the regional Sb-bearing fluids and/or igneous sulfur. The differences in S isotopic compositions of mineralization that formed during periods A and B suggest that the remobilization and overprinting caused the later-formed sulfides to partly inherit the S isotopic composition of the early-formed Pb–Zn sulfides by mixing of sulfur from two different sources. In other words, S of sulfides in period B could be a mixing S sources, consisting from pre-existing sulfides and the regional Sb-bearing fluids and/or igneous.

The carbonaceous slates around the Zhaxikang area are radioactive and contain U and Th concentrations of 11400–16500 ppb and 1390–1700 ppb, respectively, and with sulfides that contain Th and U concentrations of 14–81 ppb and 4–37 ppb, respectively (Zhang Jianfang et al., 2010). The highly radiogenic nature of the Pb within sulfides in the study area suggests some of this Pb was derived from wall-rocks. It appears that the overprinting Sb-rich fluid contained high concentrations of Pb, resulting in a detectable influence of the newly introduced fluid on the Pb isotope composition of recrystallized galena, sphalerite, sulfosalt minerals, and stibnite. The linear trend defined by these samples (Fig. 17) implies mixing between pre-existing Pb–Zn sulfides and radiogenic lead supplied by the later mineralizing event that was associated with the formation of regional Sb-quartz veins (e.g., the Lamuyouta quartz–stibnite veins; Du Zehong et al., 2011), in a similar model as that proposed for the Ramsbeck deposit in Germany (Wagner and Schneider, 2002). The more radiogenic nature of the later-formed Pb–Sb sulfosalts may relate to an increased influx of the overprinting Sb-rich fluid or a relative decrease of Pb remobilization from the early-formed and overprinted Pb–Zn sulfide veins.

## 7.2 Comparison with analogues in other orogens

The exact processes involved in remobilization and overprinting within the deposit have been outlined above. However, these processes are not unique to this deposit, as similar siderite-Pb-Zn-Cu-Sb polymetallic ore veins have been identified within the Variscan orogenic belt, in the Rheinisches Schiefergebirge district of West Germany (Wagner and Cook, 1998). The mineralization in this area has almost identical mineral assemblages, ore types, structures, textures, sphalerite Fe concentrations, and variations in S and Pb isotope compositions to those recorded in the present study area, with both deposits forming in similar tectonic settings. The Pb-Zn sulfides in the Rheinisches Schiefergebirge district formed during the Variscan period, whereas the Sb-bearing veins formed after the Variscan along tensional NW-SE- to NE-SW-striking normal faults (Wagner and Boyce, 2003). These overprinting and remobilization processes may also have formed large amounts of sulfosalt minerals in polymetallic deposits elsewhere, such as the Ramsbeck Pb-Zn-Sb deposit, also within the Rheinisches Schiefergebirge district (Wagner and Cook, 1998; Wagner and Boyce, 2001; Wagner and Schneider, 2002). This indicates that the overprinting and remobilization of ores within collisional settings also occurred in this area, where Variscan Pb-Zn orebodies were overprinted and remobilized by late-stage Sb-rich fluids during post-Variscan tectonism (Wagner and Boyce, 2001).

## 7.3 Implications for exploration

The similarities in mineralization between the siderite-Pb-Sb deposits of the late Variscan collisional orogenic belt and the polymetallic Himalayan Sb-Au-Pb-Zn metallogenic belt, indicate that overprinting and remobilization of existing mineralization is likely to be common in post-collisional settings, with pre-existing Pb-Zn sulfides acting as both chemical barriers and the source of metals for Sb-bearing fluids within such settings.

The data presented here indicate that the Himalaya is a highly prospective area for Pb-Zn exploration, primarily because it most likely hosts a belt of Pb-Zn mineralization. This exploration should also target areas hosting Sb-quartz veins, as these areas are most likely the sites of extensive overprinting and remobilization during post-collisional tectonism within the Tethyan Himalaya.

## 8 Conclusions

The discussion outlined above allows us to reach the following conclusions:

(1) The Zhaxikang deposit is the largest known polymetallic deposit in the Himalaya of southern Tibet,

and contains complex mineral assemblages and metal associations. Two distinct periods of mineralization have been recognized in the deposit; these periods are further subdivided into 6 stages and 12 substages of deposit formation. Petrographic and microthermometric data indicate that the deposit was formed by low- to medium-temperature and low-salinity ore-forming fluids that were involved in a complex series of ore-forming processes.

(2) Extensive replacement of minerals, variations in the Fe content of sphalerite, vertical and lateral changes in the grades of the main orebodies, and the S and Pb isotopic compositions of sulfides within the deposit indicate that the Zhaxikang deposit formed by remobilization of existing Pb-Zn sulfides that were also overprinted by later Sb-rich ore-forming fluids. This involved the discharge of Sb-rich fluids in a post-collisional setting, which overprinted or reworked pre-existing coarse-grained Pb-Zn sulfides (that may have already been brecciated), remobilizing some of the metals within the original sulfides (mainly Pb and Zn) that were then incorporated into Sb-rich fluids. A subsequent decrease in temperature caused the precipitation of the remobilized galena and sphalerite with sulfosalt minerals and stibnite in fault-bounded open spaces.

(3) This study outlines the potential existence of a Pb-Zn metallogenic belt within the Himalaya Orogen. This belt likely contains pre-existing Pb-Zn sulfides that could provide both a source of metals and an effective chemical barrier for later Sb-Pb-Zn mineralization during post-collisional tectonism. Zhaxikang-style deposits are also present in other collisional orogens, such as the Ramsbeck polymetallic deposit associated with the Variscan orogeny, meaning that the relationships and processes identified in the study area could guide Pb-Zn exploration in other similar orogens.

## Acknowledgements

This study was supported by grants from the Ministry of Science and Technology of China (National Key Research and Development Project of China: 2016YFC0600308), and from a Program of the China Geological Survey (DD20160015), from NSFC (41702086 & 41503040). The authors thank all of the mining engineers at Huayu Co., Ltd, who supported this study.

Manuscript received Sept. 20, 2016

accepted Sept. 23, 2017

edited by Fei Hongcai

## Reference

Armijo, R., Tapponnier, P., Mercier, J., and Tong-Lin, H., 1986.

- Quaternary extension in southern Tibet: Field observations and tectonic implications. *Journal of Geophysical Research*, 91(B14): 13803–13813.
- Bente, K., and Doering, T.H., 1995. Experimental studies on the solid state diffusion of Cu + in ZnS and on “disease”, DIS (Diffusion Induced Segregations), in sphalerite and their geological applications. *Mineralogy and Petrology*, 53(4): 285–305.
- Blisniuk, P.M., Hacker, B.R., Glodny, J., Ratschbacher, L., Bi, S., Wu, Z., McWilliams, M.O., and Calvert, A., 2001. Normal faulting in central Tibet since at least 13.5 Myr ago. *Nature*, 412(6847): 628–632.
- Bodnar R.J., 1993. Revised equation and table for determining the freezing point depression of H<sub>2</sub>O-NaCl solutions. *Geochim Cosmochim Acta*, 57: 683–684.
- Burchfiel, B.C., Chen, Z., Hodges, K.V., Liu, Y., Royden, L.H., and Deng, C., 1992. The south tibetan detachment system, himalayan orogen: extension contemporaneous with and parallel to shortening in a collisional mountain belt. *Special Paper of the Geological Society of America*, 269(21): 41.
- Burg, J.P., Guiraud, M., Chen, G.M., and Li, G.C., 1984. Himalayan metamorphism and deformations in the North Himalayan Belt (southern Tibet, China). *Earth and Planetary Science Letters*, 69(2): 391–400.
- Cogan, M.J., Nelson, K., Kidd, W., and Wu, C., 1998. Shallow structure of the Yadong-Gulu rift, southern Tibet, from refraction analysis of Project INDEPTH common midpoint data. *Tectonics*, 17(1): 46–61.
- Coleman, M., and Hodges, K., 1995. Evidence for Tibetan plateau uplift before 14 Myr ago from a new minimum age for east-west extension. *Nature*, 374(6517): 49–52.
- Debon, F., LeFort, P., Sheppard, S.M., and Sonet, J., 1986. The four plutonic belts of the Transhimalaya-Himalaya: A chemical, mineralogical, isotopic, and chronological synthesis along a Tibet-Nepal section. *Journal of Petrology*, 27(1): 219–250.
- Du Zehong, Gu Xuexiang, Li Guanqing, Zang Yongmei, Cheng Wenbin, Jing Liangbing and Zhang Xingguo, 2011. Sulfur, lead isotope composition characteristics and the relevant instrutive significance of the Lamuyouta Sb(Au) deposit, South Tibet. *Geoscience*, 25(5): 853–860 (in Chinese with english abstract).
- Duan Jilin, Tang Juxing and Lin Bin, 2016. Zinc and lead isotope signatures of the Zhaxikang Pb–Zn deposit, South Tibet: implications for the source of the ore-forming metals. *Ore Geology Review*, 78: 58–68.
- England, P., and Houseman, G., 1989. Extension during continental convergence, with application to the Tibetan Plateau. *Journal of Geophysical Research*, 94(B12): 17561–17579.
- Gao Hongxue, Li Haiping and Song Ziji, 1996. Metamorphic core complexes in southern Tibet. *Regional Geology of China*, 4:317–322 (in Chinese with English abstract).
- Guillot, S., and Le Fort, P., 1995. Geochemical constraints on the bimodal origin of High Himalayan leucogranites. *Lithos*, 35 (3): 221–234.
- Haas, J.L., 1976. Physical properties of the coexisting phases and thermochemical properties of the H<sub>2</sub>O component in boiling NaCl solutions. *US Geological Survey Bulletin*, 1421A: 1–73.
- Harris, N., and Massey, J., 1994. Decompression and anatexis of Himalayan metapelites. *Tectonics*, 13(6): 1537–1546.
- Harrison, T.M., Copeland, P., Kidd, W., and Lovera, O.M., 1995. Activation of the Nyainqentanghla shear zone: Implications for uplift of the southern Tibetan Plateau. *Tectonics*, 14(3): 658–676.
- Harrison, T.M., Copeland, P., Kidd, W., and Yin, A., 1992. Raising Tibet. *Science*. 255(5052): 1663–1670.
- Harrison, T.M., Lovera, O.M., and Grove, M., 1997. New insights into the origin of two contrasting Himalayan granite belts. *Geology*, 25(10): 899–902.
- Hauck, M., Nelson, K., Brown, L., Zhao, W., and Ross, A., 1998. Crustal structure of the Himalayan orogen at ~ 90 east longitude from Project INDEPTH deep reflection profiles. *Tectonics*, 17(4): 481–500.
- Hodges, K.V., 2000. Tectonics of the Himalaya and southern Tibet from two perspectives. *Geological Society of America Bulletin*, 112(3): 324–350.
- Hou Zengqian and Zhang Hongrui, 2015. Geodynamics and metallogeny of the eastern Tethyan metallogenic domain. *Ore Geology Review*, 70: 346–384.
- Hou, Z.Q., and Cook, N.J., 2009. Metallogenesis of the Tibetan collisional orogen: A review and introduction to the special issue. *Ore Geology Reviews*, 36(1): 2–24.
- Hou Zengqian, Qu Xiaoming, Yang Zhusen, Meng Xiangjin, Li Zhengqing, Yang Zhiming, Zheng Mianping, Zheng Youye, Nie Fengjun and Gao Yongfeng, 2006. Metallogenesis in Tibetan collisional orogenic belt: III. Mineralization in post-collisional extension setting. *Mineral deposits*, 25(6): 629–651 (in Chinese with English abstract).
- Hu Guyue, Zeng Lingsen, Chen Han and Gao Li'e, 2016. Assembling Mechanism for the Late-Miocene Mabja Leucogranite Pluton, Himalayan Orogen. *Acta Geologica Sinica*, 90(8): 1737–1754 (in Chinese with English abstract).
- Hutchison, M.N., and Scott, S.D., 1981. Sphalerite geobarometry in the Cu-Fe-Zn-S system. *Economic Geology*, 76(1): 143–153.
- Kapp, P., Yin, A., Harrison, T.M., and Ding, L., 2005. Cretaceous-Tertiary shortening, basin development, and volcanism in central Tibet. *Geological Society of America Bulletin*, 117(7–8): 865–878.
- Kumar, S., Singh, N.S., and Patil, S.K., 2016. Geochemical characteristics of proterozoic mafic dykes from the Bomdila Group of rocks, NE Lesser Himalaya, India. *Acta Geologica Sinica* (English Edition), 90(z1): 122.
- Lee, J., Hacker, B., and Wang, Y., 2004. Evolution of North Himalayan gneiss domes: structural and metamorphic studies in Mabja Dome, southern Tibet. *Journal of Structural Geology*, 26(12): 2297–2316.
- Lee, J., Hacker, B.R., Dinklage, W.S., Wang, Y., Gans, P., Calvert, A., Wan, J.L., Chen, W., Blythe, A.E., and McClelland, W., 2000. Evolution of the Kangmar Dome, southern Tibet: Structural, petrologic, and thermochronologic constraints. *Tectonics*, 19(5): 872–895.
- Leech, M.L., Singh, S., Jain, A., and Klempner, S.L., Manickavasagam, R., 2005. The onset of India–Asia continental collision: early, steep subduction required by the timing of UHP metamorphism in the western Himalaya. *Earth and Planetary Science Letters*, 234(1): 83–97.
- Li Jingao, Wang Quanhai, Chen Jiankun, Yao Peng and Peng Yongming, 2002. Study of metallogenic and prospecting models for the Shalagang antimony deposit, Gyangze, Tibet. *Journal of Chengdu University of Technology*, 29: 533–538 (in Chinese with English abstract).

- Li Zhengqing, Hou Zengqian, Nie Fengjun and Meng Xiangjin, 2005. Characteristic and distribution of the partial melting layers in the upper crust: evidence from active hydrothermal fluid in the south Tibet. *Acta geologica sinica*, 79(1): 68–76 (in Chinese with English abstract).
- Liang Wei, Hou Zengqian, Yang Zhusen, Li Zhenqing, Huang Kexian, Zhang Song, Li Wei and Zheng Yuanchuan, 2013. Remobilization and overprinting in the Zhaxikang Pb-Zn-Ag-Sb polymetal ore deposit, southern Tibet: implications for its metallogenesis. *Acta Petrologica Sinica*, 29(11): 3828–3842 (in Chinese with English abstract).
- Liang Wei, Yang Zhusen and Zheng Yuanchuan, 2015. The Zhaxikang Pb-Zn polymetallic deposit: Ar-Ar age of sericite and its geological implication. *Acta Geological Sinica*, 89(3): 560–568 (in Chinese with English abstract).
- Lin Bin, Tang Juxing, Zheng Wenbao, Wang Yiyun, Gao Yiming, Lin Xing, Yang Huanhuan, Leng Qiufeng, Li Xiaotong, Tang Xiaoqian and Fu Yangang, 2016. A preliminary study of geological features and metallogenic epoch in Keyue Zn polymetallic deposit, Tibet. *Mineral Deposits*, 35(1): 33–50 (in Chinese with English abstract).
- Liu Wenchan, Wang Yu, Zhang Xiangxin, Li Huiming, Zhou Zhiguang and Zhao Xingguo, 2004. The rock types and isotope dating of the Kangmar gneissic dome in southern Tibet. *Earth Science Frontiers*, 11(4): 491–501 (in Chinese with English abstract).
- Ludwig, K.R., 2003. User's Manual for isoplot 3.00. A geochronological toolkit for Microsoft Excel. *Berkeley Geochronology Center Special Publication 4*: 70.
- Lv Xiaochun, Ren Chong, Wu Rui, Cheng Ming, Qiu Hai and Qiu Yang, 2016. Discovery of bimodal volcanics in Longzi area, southern Xizang: Evidences from SHRIMP U-Pb zircon age and geochemical analysis. *Geological Review*, 62(4): 945–954.
- Maluski, H., Matte, P., Brunel, M., and Xiao, X., 1988. Argon 39-Argon 40 dating of metamorphic and plutonic events in the North and High Himalaya belts (southern Tibet-China). *Tectonics*, 7(2): 299–326.
- Mizuta, T., 1988. Interdiffusion rate of zinc and iron in natural sphalerite. *Economic Geology*, 83(6): 1205–1220.
- Mizuta, T., and Scott, S.D., 1997. Kinetics of iron depletion near pyrrhotite and chalcopyrite inclusions in sphalerite; the sphalerite speedometer. *Economic Geology*, 92(7–8): 772–783.
- Moles, N.R., 1983. Sphalerite composition in relation to deposition and metamorphism of the Foss stratiform Ba-Zn-Pb deposit, Aberfeldy, Scotland. *Mineralogical Magazine*, 47(345): 487–500.
- Molnar, P., and Tapponnier, P., 1978. Active tectonics of Tibet. *Journal of Geophysical Research*, 83(B11): 5361–5375.
- Mulch, A., and Chamberlain, C.P., 2006. Earth science: The rise and growth of Tibet. *Nature*, 439(7077): 670–671.
- Nie Fengjun, Hu Peng, Jiang Sihong, Li Zengqing, Liu Yan and Zhou Yongzhang, 2005. Types and temporal-spacial distribution of gold and antimony deposit( prospects) in Southern Tibet, China. *Acta Geologica Sinica*, 79(3): 373–385 (in Chinese with English abstract).
- Ohmoto, H., 1972. Systematics of sulfur and carbon isotopes in hydrothermal ore deposits. *Economic Geology*, 67(5): 551–578.
- Pan, Y., and Kidd, W.S.F., 1992. Nyainqentanglha shear zone: A late Miocene extensional detachment in the southern Tibetan Plateau. *Geology*, 20(9): 775–778.
- Qi Xuexiang, Li Tianfu, Meng Xiangjin and Yu Chunlin, 2008. Cenozoic tectonic evolution of the Tethyan Himalayan foreland fault-fold belt in southern Tibet, and its constraint on antimony-gold polymetallic minerogenesis. *Acta Petrologica Sinica*, 24(7): 1638–1648 (in Chinese with English abstract).
- Quigley, M., Liangjun, Y., Xiaohan, L., Wilson, C.J., Sandiford, M., and Phillips, D., 2006.  $^{40}\text{Ar}/^{39}\text{Ar}$  thermochronology of the Kampa dome, southern Tibet: Implications for tectonic evolution of the North Himalayan gneiss domes. *Tectonophysics*, 421(3): 269–297.
- Rui Zongyao, Li Guangming and Wang Longsheng, 2004. Metallogenic ore resources in Qinghai-Tibetan Plateau. *Geological Bulletin of China*, 23: 20–23 (in Chinese).
- Rye, R.O., and Ohmoto, H., 1974. Sulfur and carbon isotopes and ore genesis: a review. *Economic Geology*, 69(6): 826–842.
- Schärer, U., Xu, R.-H., and Allègre, C.J., 1986. U (Th) Pb systematics and ages of Himalayan leucogranites, South Tibet. *Earth and Planetary Science Letters*, 77(1): 35–48.
- Searle, M.P., Parrish, R.R., Hodges, K.V., Hurford, A., Ayres, M.W., and Whitehouse, M.J., 1997. Shisha Pangma leucogranite, south Tibetan Himalaya: Field relations, geochemistry, age, origin, and emplacement. *The Journal of Geology*, 105(3): 295–318.
- Sun Xiang, Zheng Youye, Pirajno, P., McCuaig, T.C., Yu Miao, Xia Shenlan, Song Qingjie and Chang Huifang, 2018. Geology, S-Pb isotopes, and  $^{40}\text{Ar}$ - $^{39}\text{Ar}$  geochronology of the Zhaxikang Sb-Pb-Zn-Ag deposit in South Tibet: implications for multiple mineralization events at Zhaxikang. *Mineralium Deposita*, 53(3): 435–458.
- Sun Xiaoming, Zhang Yan, Xiong Dexing, Sun Weidong, Shi Guiyong, Zhai Wei and Wang Shengwei, 2009. Crust and mantle contributions to gold-forming process at the Daping deposit, Ailaoshan gold belt, Yunnan, China. *Ore Geology Reviews*, 36(1): 235–249.
- Tapponnier, P., and Molnar, P., 1977. Active faulting and tectonics in China. *Journal of Geophysical Research*, 82(20): 2905–2930.
- Tong Jinsong, Liu Jun, Zhong Huaming, Xia Jun, Lu Rukui and Li Yunhuai, 2007. Zircon U-Pb dating and geochemistry of mafic dike swarms in the Lhozag area, southern Tibet, China, and their tectonic implications. *Geological Bulletin of China*, 26(12): 1654–1664 (in Chinese with English abstract).
- Wagner, T., and Boyce, A.J., 2001. Sulphur isotope characteristics of recrystallisation, remobilisation and reaction processes: a case study from the Ramsbeck Pb-Zn deposit, Germany. *Mineralium Deposita*, 36(7): 670–679.
- Wagner, T., and Boyce, A.J., 2003. Sulphur isotope geochemistry of black shale-hosted antimony mineralization, Arnsberg, northern Rhenish Massif, Germany: Implications for late-stage fluid flow during the Variscan orogeny. *Journal of the Geological Society*, 160(2): 299–308.
- Wagner, T., and Cook, N., 1998. Sphalerite remobilization during multistage hydrothermal mineralization events—examples from siderite-Pb-Zn-Cu-Sb veins, Rheinisches Schiefergebirge, Germany. *Mineralogy and Petrology*, 63(3–4): 223–241.
- Wagner, T., and Schneider, J., 2002. Lead isotope systematics of vein-type antimony mineralization, Rheinisches

- Schiefergebirge, Germany: A case history of complex reaction and remobilization processes. *Mineralium Deposita*, 37(2): 185–197.
- Wang Da, Sun Xiang, Zheng Youye, Wu Song, Xia Shenlan, Chang Huifang and Yu Miao, 2017. Two pulses of mineralization and genesis of the Zhaxikang Sb-Pb-Zn-Ag deposit in southern Tibet: Constraints from Fe-Zn isotopes. *Ore Geology Reviews*, 84: 347–363.
- Wang Yaying, Zeng Liseng, Zhao Linghao and Shang Zhen, 2016. Multiple phases of mafic magmatism in Gyangze-Kangma area: Implications for the tectonic evolution of eastern Tethyan Himalaya. *Acta Geologica Sinica* (English Edition), 90(z1): 129–130.
- Xie Yuling, Li Lamei, Wang Bogong, Li Guangming, Liu Hongfei, Li Yingxu, Dong Suiliang and Zhou Junjie, 2017. Genesis of the Zhaxikang epithermal Pb-Zn-Sb deposit in southern Tibet, China: Evidence for a magmatic link. *Ore Geology Reviews*, 80: 891–909.
- Yang Zhusen, Hou Zengqian, Gao Wei, Wang Haiping, Li Zhenqing, Meng Xiangjin and Qu Xiaoming, 2006. Metallogenic characteristics and genetic model of antimony and gold deposits in southern Tibetan detachments system. *Acta Geologica Sinica*, 80(9): 1377–1391 (in Chinese with English abstract).
- Yang Zhusen, Hou Zengqian, Meng Xiangjin, Liu Yingchao, Fei Hongcai, Tian Shihong, Li Zengqing and Gao Wei, 2009. Post-collisional Sb and Au mineralization related to the South Tibetan detachment system, Himalayan orogen. *Ore Geology Reviews*, 36(1–3): 194–212.
- Yin Xiuzhang and Hu Aizhen, 2004. A tentative discussion on the genesis of some Pb-Zn deposits in western Henan based on typomorphic characteristics of sphalerite. *Geophysical and Geochemical Exploration*, 28(5): 413–417 (in Chinese with English abstract).
- Yin, A., 2000. Mode of Cenozoic east-west extension in Tibet suggesting a common origin of rifts in Asia during the Indo-Asian collision. *Journal of Geophysical Research*, 105(B9): 721745–721759.
- Yin, A., and Harrison, T.M., 2000. Geologic evolution of the Himalayan-Tibetan orogen. *Annual Review of Earth and Planetary Sciences*, 28(1): 211–280.
- Yin, A., Kapp, P.A., Murphy, M.A., Manning, C.E., Harrison, M.T., Grove, M., Ding, L., Deng, X.G., and Wu, C.M., 1999. Significant late Neogene east-west extension in northern Tibet. *Geology*, 27(9): 787.
- Zartman, R., and Doe, B., 1981. Plumbotectonics—the model. *Tectonophysics*, 75(1): 135–162.
- Zaw, K., Peters, S.G., Cromie, P., Burrett, C., and Hou, Z., 2007. Nature, diversity of deposit types and metallogenic relations of South China. *Ore Geology Reviews*, 31(1): 3–47.
- Zeng Linsen, Liu Jing, Gao Li'e, Xie Kejia and Wen Li, 2009. Early Oligocene anatexis in the Yardoi gneiss dome, southern Tibet and geological implications. *Chinese Science Bulletin*, 54(1): 104–112 (in Chinese with English abstract).
- Zhai Wei, Sun Xiaoming, Yi Jiazhou, Zhang Xiangguo, Mo Ruwei, Zhou Feng, Wei Huixiao and Zeng Qinggao, 2014. Geology, geochemistry, and genesis of orogenic gold-antimony mineralization in the Himalayan Orogen, South Tibet, China. *Ore Geology Reviews*, 58(1): 68–90.
- Zhang Jianfang, 2010b. *The genesis study of Zhaxikang lead-zinc-antimony-silver deposit, North Himalaya*. Wuhan: China University of Geosciences (M.S. thesis): 1–109 (in Chinese with English abstract).
- Zhang Jianfang, Zheng Youye, Zhang Gangyang, Gao Shengbao, Ye Xianren, Zhang Zong, Liu Minyuan and Li Jijiu, 2010a. Genesis of Zhaxikang Pb-Zn-Sb-Ag deposit in northern Himalaya: constraints from multi-isotope geochemistry. *Earth Science-Journal of China University of Geosciences*, 35(6): 1000–1011 (in Chinese with English abstract).
- Zhang Jinjiang, Yang Xiongying, Qi Guowei and Wang Dechao, 2012. Geochronology of the Malashan dome and its application in formation of the southern Tibet detachment system (STDS) and northern Himalayan gneiss domes (NHGD). *Acta Petrologica Sinica*, 27(12): 3535–3544 (in Chinese with English abstract).
- Zheng Youye, Liu Minyuan, Sun Xiang, Yuan Enhui, Tian Liming, Zheng Haitao, Zhang Gangyang and Zhang Lihua, 2012b. Type, Discovery process and significance of Zhaxikang antimony polymetallic ore deposit, Tibet. *Earth Science-Journal of China University of Geoscience*, 37(5): 1003–1014 (in Chinese with English abstract).
- Zheng Youye, Sun Xiang, Tian Liming, Zheng Haitao, Yu Miao, Yang Wantao, Zhou Tiancheng and Geng Xuebing, 2014. Mineralization, deposit type and metallogenic age of the gold antimony polymetallic belt in the eastern part of north Himalayan. *Geotectonica et Metallogenia*, 38: 108–118 (in Chinese with English abstract).
- Zheng Yuanchuan, Gu Lianxing, Tang Xiaoqian, Wang Zijiang, Wu Changzhi, Zhang Wenlan and Wu Xueyi, 2012. Sulfide remobilisation from sulfide ore at high temperatures and differential stresses: An experimental approach. *Resource Geology*, 62(2): 174–186.
- Zhou Qing, Li Wencan, Qing Chengshi, Lai Yang, Li Yingxu, Liao Zhenwen, Wu Jianyang, Wang Shengwei, Donglei and Tian Enyuan, 2017. Origin and tectonic implications of the Zhaxikang Pb-Zn-Sb-Ag deposit in northern Himalaya: Evidence from structures, Re-Os-Pb-S isotopes, and fluid inclusions. *Mineralium Deposita*, 2017: 1–16.
- Zhu Dicheng, Mo Xuanxue, Pan Guitang, Zhao Zhidan, Dong Guocheng, Shi Yuruo, Liao Zhongli, Wang Liquan and Zhou Changyong, 2008. Petrogenesis of the earliest Early Cretaceous mafic rocks from the Cona area of the eastern Tethyan Himalaya in south Tibet: Interaction between the incubating Kerguelen plume and the eastern Greater India lithosphere? *Lithos*, 100(1): 147–173.

#### About the first author

LIANG wei male; born in 1986 in Weiyuan City, Sichuan Province; Ph. D; graduated from China University of Geosciences; He is now interested in the study on metallogenesis of Southern Tibet. Email: lwcugb@126.com; phone: 13810985990.